

2009-01-01

Characterization Of A Mems Accelerometer For A Highway Health Monitoring Ultra-Low Power Sensor

Karla Cecilia Enriquez

University of Texas at El Paso, kcenriquez@miners.utep.edu

Follow this and additional works at: https://digitalcommons.utep.edu/open_etd



Part of the [Civil Engineering Commons](#), and the [Electrical and Electronics Commons](#)

Recommended Citation

Enriquez, Karla Cecilia, "Characterization Of A Mems Accelerometer For A Highway Health Monitoring Ultra-Low Power Sensor" (2009). *Open Access Theses & Dissertations*. 248.

https://digitalcommons.utep.edu/open_etd/248

This is brought to you for free and open access by DigitalCommons@UTEP. It has been accepted for inclusion in Open Access Theses & Dissertations by an authorized administrator of DigitalCommons@UTEP. For more information, please contact lweber@utep.edu.

CHARACTERIZATION OF A MEMS ACCELEROMETER FOR A
HIGHWAY HEALTH MONITORING ULTRA-LOW POWER SENSOR

KARLA CECILIA ENRIQUEZ

Department of Electrical and Computer Engineering

APPROVED:

Eric MacDonald, Ph.D., Chair

Scott Starks, Ph.D.

Eric Freudenthal, Ph.D.

Patricia D. Witherspoon, Ph.D.
Dean of the Graduate School

Copyright ©

by

Karla Cecilia Enriquez

2009

Dedication

This thesis is dedicated to my family.

DEVELOPMENT OF AN ULTRA-LOW POWER SENSOR FOR HIGHWAY HEALTH MONITORING

by

KARLA CECILIA ENRIQUEZ, B.S. EE

THESIS

Presented to the Faculty of the Graduate School of

The University of Texas at El Paso

in Partial Fulfillment

of the Requirements

for the Degree of

MASTER OF SCIENCE

Department of Electrical and Computer Engineering

THE UNIVERSITY OF TEXAS AT EL PASO

August 2009

Acknowledgements

I would like to thank my advisor and committee chair, Dr. Eric MacDonald for his continued guidance and support. Dr. MacDonald's commitment to student success has opened the door to valuable learning experiences and professional opportunities, and his enthusiasm and confidence have been sources of encouragement throughout my time as a graduate student.

I would also like to thank Dr. Scott Starks for his participation and support. His encouragement and assistance have had a great influence in my academic and professional development.

I also wish to thank Dr. Eric Freudenthal for taking an interest in the project. His input and support are greatly appreciated.

For his collaboration and for providing the opportunity for me to work on this project, thanks to Dr. Soheil Nazarian.

Special thanks to James Myers and Sergio Rocha. The completion of this project would have not been possible without their valuable suggestions and assistance with the concepts and equipment involved in the testing procedure.

Additionally, I would like to thank Ralph Loya for providing his time and the resources necessary to complete a functional prototype.

Finally I would like to express my heartfelt gratitude to all my family. Thanks to my mother, for her love and dedication are constant sources of strength. Thanks also to Esther and Ezequiel Lopez for their invaluable support. Their hard work has been a source of inspiration. I would like to specially thank my husband, Antonio Lopez for all his love, words of encouragement, and hard work.

Abstract

With the 2009 American Recovery and Reinvestment Act, government officials recognized the need to implement automated methods that reduce the cost of assessment projects and provide a long-term solution to monitor the structural health of bridges and highways. Although important research exists in the area of non-destructive evaluation, current road health monitoring efforts continue to be costly and time consuming. This thesis focuses on the characterization of a MEMS accelerometer intended to be the basis of a novel ultra-low power sensing system to remotely assess the condition of highways. The architecture of a sensor prototype built to validate an algorithm to obtain displacement figures from acceleration data is described. Results show that the sensor prototype successfully produces figures proportional to displacement at frequencies between 5 and 30 Hz. The layout of an AISC is presented as an ultra-low power alternative to components currently used in the design of wireless sensors.

Table of Contents

Acknowledgements.....	v
Abstract.....	vi
Table of Contents.....	vii
List of Tables.....	ix
List of Figures	x
Chapter 1: Introduction	1
Chapter 2: Structural Health Monitoring Overview	4
2.1 The use of MEMS in SHM Applications	5
2.2 RF Energy Harvesting for SHM Wireless Sensors	7
Chapter 3: Previous Work.....	10
Chapter 4: Proposed Sensor Prototype for Highway Health Monitoring	31
4.1 Proposed Architecture of the Sensor Prototype.....	31
4.2 Power Consumption of the Sensor Prototype.....	33
4.3 Design Parameters for the ADXL202	34
4.3 Double Integration Algorithm	40
4.4 Sensor Prototype Validation.....	45
4.5 Sine Vibration Testing.....	47
Chapter 5: Results.....	49
5.1 Experimental Results.....	49
5.2 ASIC Layout.....	61
Chapter 6: Conclusion and Future Work	64
6.1 Conclusion	64
6.2 Future Work.....	65

Works Cited.....	66
Appendix A: Verilog Code	70
Appendix A: Verilog Code	70
Appendix B: ASIC Reports.....	77
Vita	81

List of Tables

Table 4.1: Power Characteristic of the Sensor Prototype.	34
Table 4.2: Filter Capacitor Selection C_x , C_y	36
Table 4.3: Typical Noise Output for the ADXL202.....	37
Table 4.4: Parameter Values for Sinusoid Vibration Testing.	48
Table 5.1: ASIC Detail Summary.....	62
Table 5.2: Power Characteristics of the Ultra-Low Power Sensor.....	63

List of Figures

Figure 1.1: Proposed Highway Health Monitoring System.....	2
Figure 2.1: Powercast RF Energy Delivery.....	9
Figure 3.1: WiMMS Architecture.....	11
Figure 3.2: WiMMS Dual Core Architecture.....	13
Figure 3.3: Kotappalli's Architecture of the Local Site Master and Sensing Unit.....	15
Figure 3.4: WISAN Node.....	18
Figure 3.5: Wang's Architecture of a Low-Power Sensing Unit Prototype.....	19
Figure 3.6: (a) Hardware and (b) Software Architecture of Sukun's Sensing Platform.....	23
Figure 3.7: RFID-based Strain Sensor.....	26
Figure 4.1: Architecture of the Sensor Prototype.....	32
Figure 4.3: Orientation of the ADXL202.....	39
Figure 4.4: Integral of $X = f(t)$ from T_0 to T_1	42
Figure 4.5: Verilog Algorithm to Perform Accumulation.....	44
Figure 4.6: Laboratory Validation Setting.....	46
Figure 4.7: Sensor Prototype in the Laboratory Validation Setting.....	46
Figure 4.8: Phase Relation of Acceleration, Velocity, and Displacement.....	48
Figure 5.1: (a) Acceleration (b) Velocity Lacking Initial Condition Offset After First Accumulation and (c) Accrued Initial-condition Error after Second Accumulation.....	53
Figure 5.2: 15 Hz (a) Acceleration (b) Velocity and (c) Displacement over One Period.....	55
Figure 5.3: Displacement at (a) 5 Hz (b) 10 Hz (c) 15 Hz (d) 20 Hz (e) 25 Hz and (f) 30 Hz.....	59
Figure 5.4: Displacement at (a) 1Hz and (b) Effects of the ADXL202 Noise Floor.....	60
Figure 5.5: AISC Layout.....	61

Chapter 1: Introduction

The 2006 Conditions and Performance Report issued by the Federal Highway Administration (FHA) highlighted the 50th anniversary of the Interstate Highway System (IHS). Describing the IHS as “the backbone of transportation and commerce in the United States”, the report also called for a considerable increase in funding for rehabilitation projects aimed at preserving the physical and operational conditions of urban interstate roads. Recently, major funds were allocated for traffic infrastructure maintenance and development as part of The American Recovery and Reinvestment Act of 2009 (ARRA). Taking into consideration the FHA report, the ARRA recognizes the need to implement innovative automated methods that reduce the cost of assessment projects and provide a long-term solution to monitor the structural health of bridges and highways.

Although a significant amount of research exists in the area of non-destructive evaluation, current road health monitoring efforts continue to be costly and time consuming. Traditional methods to determine the health of roads are based on visual inspection of the pavement via video and image analysis or direct human inspection (Yu, Yu 2006). These techniques are not only inefficient, in terms of the time spent evaluating a few miles of pavement, they are also subject to error as they monitor only the damage apparent on the surface of the road. More sophisticated methods make use of ultrasonic testing and ground penetrating radars to analyze the structural integrity of roads. These systems, however, require expensive equipment and trained professionals to carry out the evaluation process.

Taking advantage of the recent advances in the development of wireless sensors for Structural Health Monitoring (SHM) applications, a long-term monitoring system has been proposed to rapidly and remotely assess the structural health of highways. At the University of

Texas at El Paso, Civil Engineering professor Dr. Soheil Nazarian revealed that the analysis of strain and displacement experienced by a road under dynamic traffic loading provides an effective measure of the structural integrity of the pavement. Based on his conclusions, new ideas for a monitoring system include the use of a weight calibrated truck to induce vibrations on a road under evaluation. A vibration sensor embedded beneath the surface of the pavement records and process acceleration data as the vehicle drives overhead. Maximum displacement figures derived from acceleration data are then transmitted wirelessly to the test vehicle within a second. The proposal considers the use of RFID energy transmitted by the test vehicle a few seconds prior to the acquisition of data to power the wireless sensor (fig. 1.1). A key element of this initiative is the incorporation of techniques to significantly reduce the power consumption of the wireless sensor. The reduction of energy allows the use of harvested RFID power to make this a long-term alternative to monitor the health of roads.



Figure 1.1: Proposed Highway Health Monitoring System.

Building upon these ideas, this thesis focuses on the characterization of a MEMS accelerometer intended to be the basis of an ultra-low power sensor for this long-term highway health monitoring system. The paper briefly describes the applications of SHM research and

explores the incorporation of RFID energy harvesting and the use of Micro-Electro-Mechanical Systems (MEMS) in these applications. An overview of the development of wireless sensors to monitor the health of structures over the last decade is also provided. The thesis presents the architecture of a sensor prototype built to validate an algorithm used to obtain peak-to-peak displacement figures from acceleration data. It also describes the process followed to test this prototype in a laboratory setting. To address the issue of power consumption, the layout of an Application Specific Integrated Circuit (ASIC), that implements the displacement algorithm, is presented as an ultra-low power alternative to commercially available devices currently used in the design of wireless sensors. Finally, the concluding chapter discusses the limitations of the design and suggests possible solutions to be explored in the future. As a whole, this project provides an important component in the development of a new long-term system to quickly assess the health of roads, reduce the cost of evaluation, and ensure the efficient use of funding for highway rehabilitation projects.

Chapter 2: Structural Health Monitoring Overview

The field of Structural Health Monitoring (SHM) is an active research area dedicated to the development of novel technologies to detect and assess damage in order to ensure the construction and maintenance of safe structures. These technologies combine the use of autonomous systems and damage detection algorithms to record and analyze the behavior of structures such as buildings, bridges, aircrafts and ships (Lynch *et al.* 2006).

Damage detection methods used in SHM can be classified into two types: local damage detection and global damage detection techniques (Chintalapudi 2006). Local methods focus on the study of specific faults present on a determined area or component of the structure. These methods make use of sophisticated thermal, magnetic, x-ray, ultrasound and optical imaging technologies to analyze structural faults, and require the use of expensive equipment and trained professionals to assess the results. Global damage detection techniques, on the other hand, are aimed at identifying damage that is significant enough to alter the properties of major sections of the structure or the structure as a whole. These methods monitor the response of structures to natural or forced excitations and identify damage from the analysis of changes in the dynamic properties of the structure under evaluation.

The study of structural response to vibration is a popular technique within global damage detection methods (Hsieh 2006). The collection of vibration data leads to the analysis of modal frequencies and/or modal shapes (expected curvature or displacement) of a structure to determine if damage is present. Existent vibration analysis algorithms derive information about the modal states of a structure using time history data or data converted to the frequency domain. The sources of vibration used in damage detection methods are classified into free vibration, forced vibration, and ambient vibration. Free vibrations are those present when a body is released from

its original or “at rest” state and are the least common source of vibration for SHM. Equipment such as shakers and impulse hammers are commonly used to induce controlled vibrations and compare the response of structures to corresponding structural models and simulations. Sources of ambient vibrations include wind, seismic activity, and ground vibration caused by traffic and adjacent industries. Although an accurate analysis is made difficult by the lack of information regarding the frequency, amplitude, and duration of these vibrations, the use of ambient sources allow for long-term monitoring and data collection procedures at a low cost and with minimal or no disruption to traffic.

One of the main challenges facing the implementation of SHM techniques continues to be installation and maintenance cost associated with these systems. The use of Micro-Electro-Mechanical Systems (MEMS) and RFID energy harvesting components in the design of wireless sensor networks for SHM are two technologies currently explored as a solution to the reduction of these costs.

2.1 The use of MEMS in SHM Applications

Autonomous wireless sensor networks have emerged as an alternative to costly and labor intensive tethered SHM systems (Lynch 2006). Furthermore, the use of MEMS within wireless sensors has facilitated the growth of these networks to achieve higher placement densities at lower costs. MEMS are fabricated using techniques and materials used in the manufacturing of Integrated Circuits (IC). These manufacturing techniques allow for the integration of electrical, mechanical, optical and fluidic components on a single device of dimensions that range from a few micrometers to a millimeter (Bâzu 2007).

In addition to their minute dimensions, the capability to reliably operate in a wide range of frequencies and environmental conditions while consuming a limited amount of power makes

MEMS accelerometers suitable for low-energy vibration monitoring applications. The reliability of commercially available MEMS accelerometers was recently studied with a procedure introduced by Bâzu *et al.* to perform Quantitative Accelerated Life Testing (QALT) on these devices. The QALT procedure was designed as an application-driven test plan which combined thermal test and two types of mechanical stress tests: vibration and tilt. The accelerometers were tested at a fixed frequency of 1500 Hz and amplitude of 6g at temperatures of up to 145°C. The results of the tests showed excellent reliability for both vibration and tilt tests at high temperatures. With no failures encountered even after 200 hours of vibration testing at 145°C, a worst case scenario was developed. This approach assumed a failure after 201 hours of vibration monitoring at 145°C, with the fatigue fracture of the moving component of the accelerometer considered as the most likely failure source.

2.1.1 The ADXL202

Thanks to the low cost and low-power operation of this MEMS accelerometer, the ADXL202 is found in a number of designs of wireless sensors for SHM applications. The ADXL202 is a 2-axis MEMS accelerometer capable of detecting dynamic and static acceleration with a full range of $\pm 2g$. The device produces analog voltage outputs as well as a digital signal per axis whose duty cycle is proportional to acceleration. The sensor is a surface micromachined polysilicon structure assembled on top of a silicon wafer. The sensor surface is suspended above the silicon wafer with polysilicon springs that offer resistance against acceleration forces. A differential capacitor made up of independent fixed plates and central plates attached to the moving component is used to measure the deflection of the structure in response to acceleration. Deflection of the beam under acceleration forces unbalances the capacitor and produces an output square wave whose amplitude is proportional to acceleration. This signal is then rectified

and the direction of the acceleration is determined with the use of phase sensitive demodulation techniques. A duty cycle modulator stage produces the digital output at each of the pins corresponding the x and y axes.

Sensor architectures for SHM applications that include the ADXL202 are discussed in the previous work section of this paper. Moreover, chapter 4 describes the design procedure for the ADXL202 followed in the development of the sensor prototype presented in this thesis.

2.2 RF Energy Harvesting for SHM Wireless Sensors

The use of batteries to power wireless sensor units for SHM applications continues to present challenges arising from the cost and labor associated with replacing the power source of inaccessible sensors and scaled sensor networks made up of thousands of nodes. A recent article published by ON World, a leader in wireless technology research, estimates the labor costs of replacing batteries of wireless sensor networks worldwide between 2006 and 2015 at \$1.1 billion dollars. As a result, the incorporation of Radio Frequency (RF) energy transmission and the corresponding RF energy harvesting circuits in the designs of wireless sensors is currently explored as an alternative continuous power source for rechargeable and on-demand wireless sensor designs.

2.2.1 Theory behind RF Energy Transmission

The design of circuits to transmit and harvest RF energy is based on equations that describe the transmission of RF waves, the wavelength of the radiation, and the energy stored in a capacitor. The transmission of RF energy is explained by the Friis formula presented in equation 1.

$$P_R = \frac{G_T G_R \lambda^2}{(4\pi R)^2} P_T \quad (1)$$

In this equation, PR represents the amount of power received; GT is the gain of the transmitter antenna, GR is the gain of the receiver antenna; λ is the wavelength of the energy radiation; R is the distance between the antennas; and PT represents the amount of power transmitted. The wavelength of the energy transmission is obtained from the speed of light c and the frequency f of the transmitted signal, as given in equation 2.

$$\lambda = \frac{c}{f} \quad (2)$$

After the power is PR is rectified to provide a DC voltage, capacitor is used to store the energy at the receiving antenna. The amount of energy stored in a capacitor is described by equation 3.

$$E = \frac{1}{2} CV^2 \quad (3)$$

The time required to accumulate the energy necessary to charge a capacitor can be calculated as the ratio of equation 3 and equation 1.

$$Time \text{ (seconds)} = \frac{E}{P_R} \quad (4)$$

2.2.2 Commercially Available Technology for RF Energy Harvesting

A leader in the development of proprietary methods for the delivery of wireless power, Powercast offers RF energy harvesting technology for the use of wireless sensors in applications including SHM. Powercast technology features high efficiency transmitters and receivers designed to deliver a controlled source of power for battery-free SHM wireless sensors that operate continuously, on-demand, or on a scheduled basis (fig 2.1).

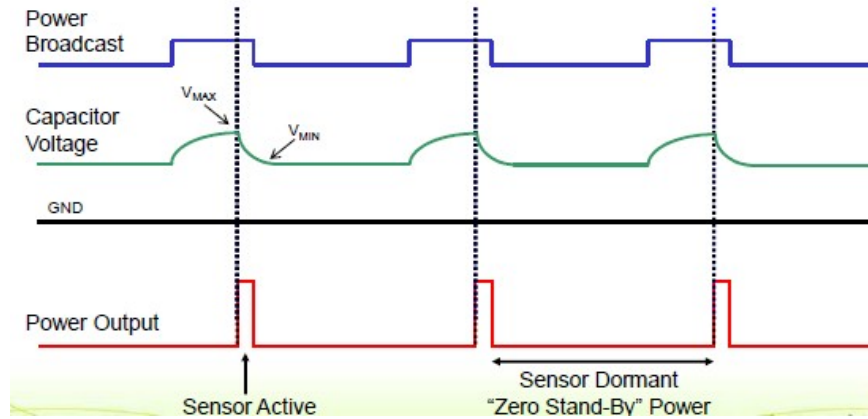


Figure 2.1: Powercast RF Energy Delivery.

The current battery-free reference system is built around the P1200 Powerharvester module in combination with a CAP-XX GZ115 supercapacitor. Using 3W sleeve-dipole antennas, this design is capable of delivering 18.5 mJ of usable energy in 145 seconds at a distance 20 ft.

A discussion of RF energy harvesting technology for SHM wireless sensors implemented in academic research is included in the previous work section of this paper.

Chapter 3: Previous Work

A variety of academic papers exploring the design and validation of sensor units and sensor networks for Structural Health Monitoring have been published over the last ten years. This section presents a review of previous research work on the development of SHM sensing systems for roads, the reduction of power consumption of sensing units, the use of MEMS accelerometers and sensor transducers, as well as the application of RFID energy as a source of power for SHM systems.

Bennett *et al.* (1999) propose the development of a wireless unit intended to monitor fatigue in pavement. The monitoring unit is designed to measure temperature and strain changes while embedded in flexible asphalt highway surfaces. The embedded monitoring core is made up of a 4-channel sensing interface, a processing core, and a communication unit. The sensing interface is based on a 16-bit ADC that samples data from two thermometer and two strain gauges. The interface also includes Wheatstone bridge and amplification circuits. The measurement data is encoded with a Hitachi H8/329 8-bit microcontroller, and routines to control the operation of the unit are stored in 32kB of external ROM. Highway response data is transmitted to a data logger on the side of the road using a narrow-band 418 MHz Radiometrix wireless radio. The radio is capable of transmitting data at up to 40 kbps over 300m.

The design represents a low-cost non-destructive alternative to tethered road health monitoring systems. The power supply used in this design, however, makes the system inadequate for lifetime monitoring of roads. Relying on four AA batteries to provide power to the unit, the authors conclude that the lifetime of the unit can reach six months operating at 6V.

In a series of papers discussing the development and validation of a novel wireless system, Lynch *et al.* (2001, 2002a, 2002b) introduce a design aimed at monitoring structural

response to ambient vibrations and seismic activity. The design, named Wireless Modular Monitoring Systems (WiMMS) emphasizes the importance of using independent monitoring units and decentralized data-acquisition and processing for the implementation of damage detection routines in real time.

The architecture presented by Lynch *et al.* is also divided into three main functional blocks: a sensing interface, a computational core, and a circuit for wireless communications. The sensing interface of this design allows an analog input between 0 and 5 V, which can be sampled at a rate of up to 1000 kHz using a single-channel, low-noise Texas Instrument 16-bit ADC. Also included as part as the sensing interface is an Analog Devices dual-axis ADXL210 accelerometer with digital outputs. An 8-bit Atmel AVR AT90S8515 enhanced RISC microcontroller is selected as the computational core because of the relatively low cost and power consumption, and the processing power of the device. Among other features, this microcontroller includes 8kB of programmable flash, 512 bytes of SRAM, and 512 bytes EEPROM used to store operational routines. The low-power spread spectrum Proxim RangeLAN2 radio modem provides a robust and reliable communication channel from unit to unit as well as between monitoring units and a base station. A functional diagram of the WiMMS is shown in Figure 3.1.

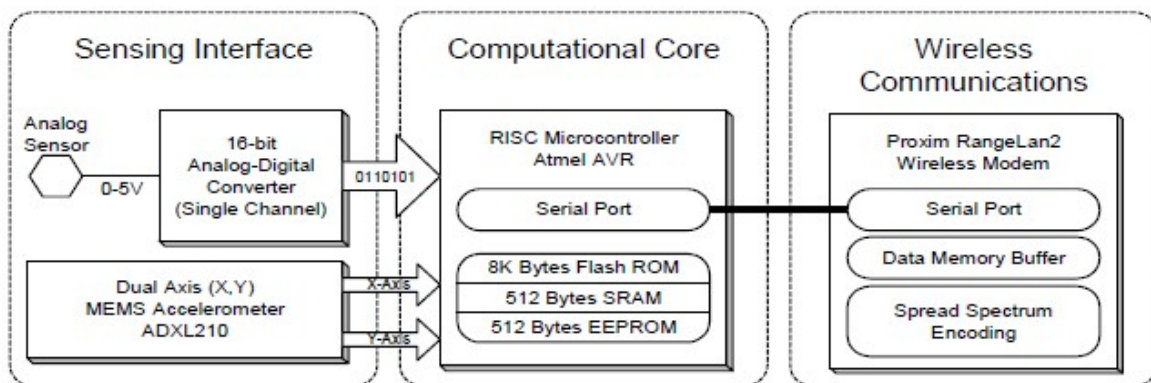


Figure 3.1: WiMMS Architecture.

The performance of the MEMS accelerometers and the use of embedded local processing routines were validated using a test structure under frequency-sweep sine excitation. The five-story aluminum test structure is mounted on a lateral shaker table vibrating at frequencies between 0.23 Hz to 3 Hz over 60 seconds. Both time domain and frequency response data closely matched the theoretical model developed for the structure. Moreover, the frequency response function of the ADXL210 was found to be less noisy than that of the high-performance piezoelectric accelerometers used in the test.

Based on the results of additional tests used to validate individual components, the authors acknowledge the limitations imposed by the use of batteries to power the monitoring unit. The sensing interface and computational core of the design together consume close to 250mW of power, and the entire unit consumes close to 1.7W during transmission. Using a 9V battery the circuit alone can operate for 20 hours. The Proxim RangeLAN2 can operate for 2.25 hours when transmitting, and up to four hours in sleep mode. These results lead the authors to the conclusion that power consumption is a critical design element that needs to be revisited in future prototypes.

Continuing their work in the development of a wireless sensing unit for WiMMS deployment, Lynch *et al.* (2003, 2004) propose a dual-core design to address the issue of power consumption. While the sensing interface and wireless communication circuits remain unchanged, the new design of the computational core includes two processors: an 8-bit Atmel AT90S8515 AVR microcontroller and the 32-bit Motorola MPC555 PowerPC microcontroller. The functional diagram for the new design is presented in Figure 3.2. Selected because of its low-cost, power efficiency, and processing capability the 8-bit Atmel microcontroller performs data-acquisition and overall operation tasks. The execution of sophisticated data interrogation

routines is left to the 32-bit Motorola microcontroller, which has the capability to quickly perform floating-point operations and includes 448 Kbytes of flash ROM and 26 Kbytes of RAM.

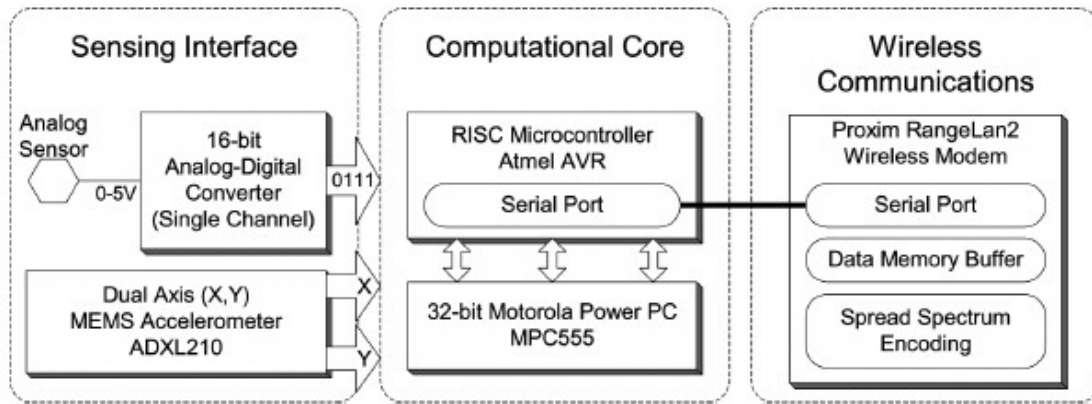


Figure 3.2: WiMMS Dual Core Architecture.

In addition to laboratory tests using the aluminum test structure described above, the new prototype is deployed on the Alamosa Canyon Bridge located in Truth or Consequences, New Mexico. The purpose is to compare the performance of the wireless monitoring unit against the Dactron SpectraBook dynamic signal analyzer, a commercially available tethered structural monitoring system. In this case, the wireless prototype is interfaced with a ± 1 g Crossbow CXL01LF1 MEMS capacitive accelerometer selected for its sensitivity and noise floor. The Dactron SpectraBook system uses the Piezotronics PCB336C accelerometer. During the first test the bridge is repeatedly excited with an impulse produced by a modal hammer at the center of the bridge deck. The time-history data and frequency response function from both accelerometers show strong similarities, with a few exceptions at very low frequencies. The time-history data from the Crossbow CXL01LF1 accelerometer, collected during a second vibration test using dynamic traffic loading, is also in agreement with the data collected from the tethered system.

Taking advantage of the dual-core architecture and the sleep-mode feature of the most power-expensive components, the authors successfully increase the operating life-time of the wireless monitoring system relative to their previous design. For this design, Lynch et.al have reduced the operating voltage of the unit to 7.5V. In addition, the low-power 8-bit microcontroller is the only component kept in active mode, while the Power PC is awake only during the execution of data processing routines and the transmission of data is carried out after all processing is done. With this new design, the unit consumes between 1.6W and 1.65W of power while processing or transmitting data. Using a 5 AA Lithium Cell battery pack, the circuit alone can operate for 50 hours with the PowerPC in sleep mode and 15 hours while active. The life-time of the wireless communication module is extended to 15 hours of continuous activity.

Kottapalli *et al.* (2003) present a two-tier wireless monitoring network as a solution to main challenges in SHM, such as time synchronization and limited power availability. The purpose of the network is to monitor real-time structural response to extreme events and intermittent monitoring of ambient loading response. The lower-tier of the network is made up of a Local Site Master (LSM) and a number of Sensing Units (SU) in close proximity. Figure 3.3 shows a block diagram for both the SUs and LSM architectures.

Each of the sensing units is based on an 8-bit ATMEL AVR microcontroller, and it is responsible for collecting vibration data using an ADXL210 high g accelerometer, a high sensitivity Model 1221 accelerometer, and a 16-bit ADC. A low-power BlueChip EVK915 915 MHz radio transceiver is used for short-range spread spectrum communication between SUs and the LSM. A network of LSMs represents the upper tier of the design and is responsible for routing the data received from SUs to a Central Site Master (CSM). Each LSM includes an 8-bit Microchip PIC microcontroller with enough memory for data storage, as well as a 915 MHz

radio transceiver for lower-tier communication, and a 2.4 GHz high data-rate radio transceiver to communicate with the CSM and other LSMs. Low data-rate communication between LSMs is also used to synchronize local units to a global clock, therefore ensuring the acquisition of synchronized time-history data. With this architecture and using 10Mbps wireless data rates, the authors predict that the size of a network for real-time SHM can reach up to 2000 to 4000 sensors with a single CSM.

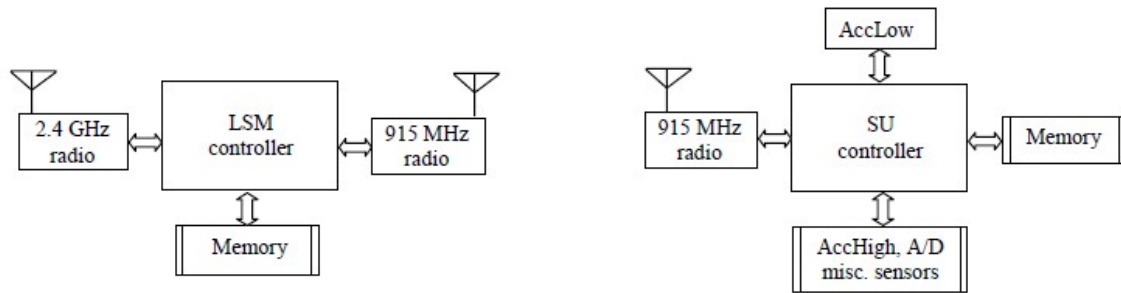


Figure 3.3: Kotappalli's Architecture of the Local Site Master and Sensing Unit.

Two laboratory test scenarios are set up to validate the performance of a two-cluster network. For the first test, aimed at simulating the use of the network for periodic structural health monitoring, all master and sensing units are powered on and each SU listens for a trigger signal from the corresponding LSM. Upon receiving the trigger signal, the sensing units acquire and transmit a determined number of samples. During a second test the wireless network is used to monitor the response to an extreme event. In this case, all sensing units start at an idle state and initiate collection of data after the measured acceleration exceeds a preprogrammed threshold. Measurement results from both tests corresponded to the vibration applied to shake the prototype units.

In addition to partitioning the computational core, Kottapalli *et al.* (2003) implement power-saving techniques in the sensor unit architecture and the communication protocol that effectively extend the life-time of the network well beyond their one-year goal. Each of the SUs

is designed to operate in one of four modes: Sleep, Update, Semi-awake and Awake. The state of the units during periodic monitoring is controlled by a schedule developed by the CSM. This schedule is created according to the environmental conditions surrounding the structure, and it ensures that only the necessary components are active. Moreover, the communication protocol used in the low-tier of the design is executed with minimum handshaking. Provided that the monitoring period does not exceed 3 minutes, a unit that is active during 5 extreme event a year, twice a day for periodic monitoring, and 12 times a day to update its schedule will consume 1600 mA hour. Using a couple of alkaline AA batteries with a 2500 mA per hour rating each, a sensing unit can operate for up to 18 months, a period after which the network will require maintenance.

Mastroleon *et al.* (2004) suggest a design of a modular wireless SHM network that improves on the power efficiency of the prototype presented by Kottapalli *et al.* (2003). The improvement is achieved by replacing some of the prototype's components by more power-efficient equivalents. One of the main modifications is the use of a Microchip PICmicro microcontroller as the basis of the computational core. The PIC micro uses multilevel priority interrupts and phase-lock loop synchronization to carry out real-time processing and time synchronization. Furthermore, the microcontroller can operate in 6 different power modes and achieve ultra-low power operation with a fail-safe clock monitor. The monitoring unit also includes self-programmable flash memory, allowing software updates through the wireless communication channel. The core of the sensing interface is a 5 channel 18-bit Maxim MAX1402 ADC. A Maxim DS18S20 digital thermometer is also included in this interface to account for the impact of changes in temperature on the quality of the measurement results.

Similarly to the design by Kottapalli *et al.* (2003), the monitoring units rely on a Bluechip RFB915B RF transceiver for wireless communication.

Sazonov *et al.* (2004) present the design of an autonomous Wireless Intelligent Sensor Network (WISAN) for Structural Health Monitoring. The network is a vibration-based monitoring system designed to detect structural damage of bridges from ambient vibration data and local changes in mode shapes, or displacement, of the structure.

The author places emphasis on the requirements for the design of a low-cost fully autonomous SHM network, and presents an architecture aimed at fulfilling these requirements. The network is organized in a two-level cluster tree fashion. In the cluster, individual sensing nodes collect vibration data and communicate wirelessly to a cluster-head that serves as a high speed router. A supernode is included in some of the clusters to provide additional computational power to execute damage detection routines on the data collected. Each data acquisition node is based on the low-power 16-bit Texas Instruments MSP430 microcontroller, and it includes a six-channel 12-bit ADC as the sensing interface, a two-channel 12-bit DAC as the actuating interface, and 4 to 16Mbits of external EEPROM for data storage. The architecture of a WISAN node is shown in Figure 3.4. Communication between nodes is achieved with a low-power Chipcon CC2420 wireless transceiver operating at 2.4GHz. The network uses the power-efficient IEEE802.15.4 wireless communication protocol designed specifically for wireless sensor networks.

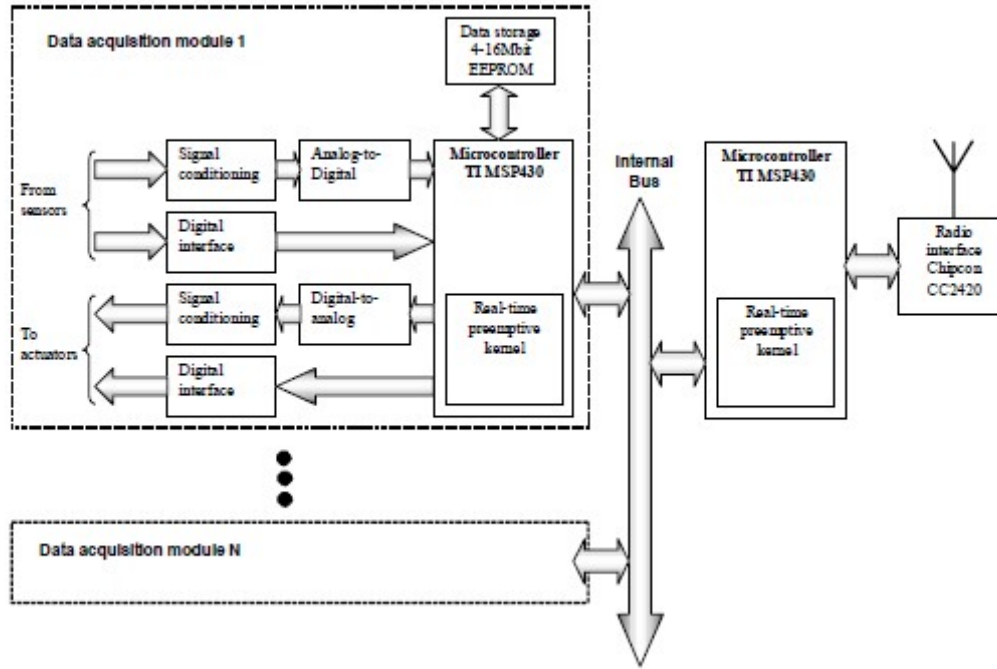


Figure 3.4: WISAN Node

In the paper, energy efficiency is one of the main considerations in the design of a low-cost fully autonomous monitoring system. Consequently, the design of the WISAN network successfully incorporates low-power components and routing techniques meant to reduce overall power-consumption. According to the author's calculations, a fully active WISAN node consumes a total of 75mW. This amount of power translates into a total of 26.45mJ of energy over a 30 second period of data acquisition at 50Hz sampling rate. Moreover, a node in low-power or inactive mode consumes only 0.1mW of power. This represents a significant improvement in energy efficiency compared to other SHM monitoring network designs, and allows for the extension of battery life-time or the use of energy-harvesting components to power the data-acquisition nodes.

A WISAN prototype has been used to test concepts address in the paper, however no laboratory or deployment implementations of the network are discussed.

Wang *et al.* (2005) introduce the design and validation of an autonomous wireless sensing system for SHM geared towards long-term monitoring of civil structures. To accomplish this, the proposed design highlights the use of components and techniques selected to reduce power consumption. Other main objectives listed by the authors include the capability for local data processing, long range communication accompanied by reliable communication protocols, high precision analog to digital conversion, peer-to-peer communication between wireless sensing units, as well as accurate and synchronized data collection at adequate sampling rates.

The prototype uses a star-topology in which a laptop or desktop computer acts as a central server that communicates with and coordinates a group of sensing units through a wireless transceiver. The individual sensing units are responsible for collecting and processing measurement data, and transferring the results of the analysis to the server. The design of the sensing units has three main components: the sensing interface, made up of a Texas Instruments ADS8341 4-channel 16-bit analog-to-digital converter with sampling rates of up to 100 kHz; a computational core, based on the low-power 8-bit Atmel ATmega128 microcontroller and 128kB of external SRAM for data storage; and a communication interface that operates in the 900 MHz spectrum using a Maxstream 9XCite wireless modem. A functional block diagram of a wireless sensing unit is presented in Figure 3.5.

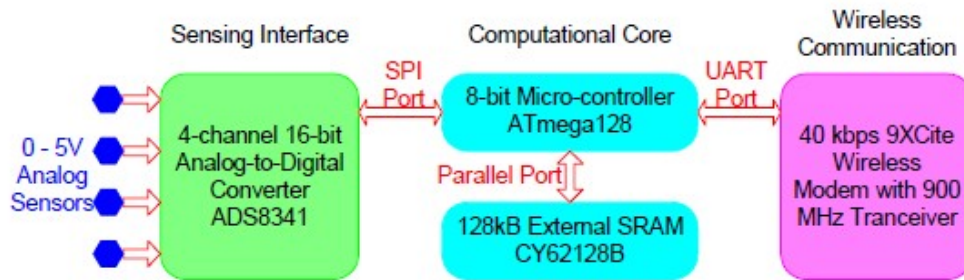


Figure 3.5: Wang's Architecture of a Low-Power Sensing Unit Prototype.

In order to coordinate data collection and transmission tasks, a multithreaded interrupt-based operating system is developed. The multithreaded quality of the software allows the sensing unit to transmit previously stored data while collecting and storing new measurement data at the same time. To ensure a reliable stream of synchronized data, the central server initiates communication by transmitting a beacon signal to all sensing units. The data collection process starts only after each sensing units has acknowledged the initial signal. The operating system also includes a feature that executes a Fast Fourier Transform (FFT) algorithm on the collected data. The frequency response information is then transmitted along with time-domain data.

The prototype is validated both in a laboratory setting and in the field. The tests performed in the laboratory focused on the validation of the frequency response function. In this case, the sensing units monitored the steady state acceleration response of a three-story aluminum test structure mounted on a shaking table. The tests show that both time-domain and frequency-domain data is successfully transmitted to the central server. Furthermore, the peak values of the frequency response correspond to the frequency of the harmonic base motion of the shaking table. Field tests to validate the performance of the wireless network were carried out on the Geumdang Bridge in Korea. On the bridge, a total of 14 wireless sensing units are placed next to units of a previously installed wire-based monitoring system. After comparing acceleration data collected over two days, it is found that time history and frequency response data from both monitoring systems have a strong one-to-one correlation. The authors conclude that, while the prototype makes the advantages of a wireless monitoring system evident, further work is required to improve noise reduction methods, sampling rates, and routines to coordinate even larger sensing networks.

The authors' selection of components and use of software to minimize wireless transmissions are successful at extending the lifetime of the monitoring system. However, the design still presents challenges for embedded structural monitoring systems. The total current of the final prototype measured in the laboratory was 77 mA during activity, and 100 μ A for an idle device. According to the authors' calculations, if a single L91 AA battery is used to power a sensing unit that is active for only five minutes a day, the total life expectancy of the system is extended to 330 days. While this represents a significant improvement for SHM systems, the cost and labor required to replace the power source of a sensing system embedded in a structure would make this an impractical alternative to current road health assessment methods.

Chung *et al.* (2004) describe the development of a palm-sized wireless unit to monitor bridge structural vibration. The main goal of the prototype is to validate the performance of the low-power ADXL202 and Silicon Design 2210 MEMS accelerometers in SHM applications. Although the names of specific components are not listed, the design of each of the monitoring units includes one of the two MEMS accelerometers in question, an analog to digital converter, a microcontroller, and an RS232 serial port to interface with a commercially available wireless transmitter.

The performance of both sensors was validated first in a laboratory setting, and the units were later tested on a pedestrian bridge at University of California, Irvine (UCI) campus. In a shaking table test at the laboratory, a 10mg sinusoid running at 2 MHz was used to excite both accelerometers. Time history plots showed that the SD 2210 performs relatively better under accelerations below 0.5mg. This difference in performance was attributed to the static noise of the ADXL202 and its associated components, which was close to 3mg. The static noise of the SD 2210 was measured at 1mg. On the field, the ADXL202, the SD 2210 and a PCB393C

tethered sensor were placed on the middle and to the side of a pedestrian bridge in order to monitor lateral and torsional motion, as well as vertical displacement and acceleration. The structural responses to three consecutive impulse excitations applied to the middle span of the bridge were analyzed in the frequency domain. The test showed that modal frequency peaks from both wireless sensors closely matched the modal frequencies identified by the traditional sensor and a simulation model. The authors conclude that, in spite of differences in noise and bandwidth, both accelerometers are successful at monitoring vibrations in this study. Furthermore, the performance of the wireless transmission was validated up to a distance of 150m.

As part of their conclusion, Chung *et al.* identify the issue of power consumption of the units as a problem that requires immediate attention. Using a 9V battery, the monitoring units ran only for only five hours. To address this issue, the authors propose the development of solar panels as a supporting power supply. These panels, combined with rechargeable battery supplies can be used to power monitoring units for more than two years.

Sukun *et al.* (2007) discuss the development of a Structural Health Monitoring platform designed to detect structural damage by way of analyzing vibration and strong motion measurements of civil structures. The authors present this design as a low-cost alternative to current hard-wired piezoelectric systems. The monitoring system is the largest multi-hop network installed on a civil structure, and its development provides important information on the challenges inherent to the deployment to real-world structures, the scalability of SHM networks, and the requirements to acquire high-quality data.

Similar to previous designs, the network is made up of several data-acquisition nodes that communicate wirelessly to a base station. Each node includes a Crossbow MicaZ mote, which

operates as the sensing interface and communication module, and an accelerometer sensor board designed for SHM applications. The board features four accelerometer channels measuring two-directions and two different accelerometers. The Silicon Designs 221L accelerometer is used to monitor low-amplitude vibrations from traffic and wind loading, while the ADXL202 dual-axis accelerometer is used to measure stronger vibrations such as the ones caused by seismic activity.

The software architecture for this network was designed to address major requirements for data-collection and transmission. The design is based on TinyOS operating system and it uses an application called Structural hEalth moNiToRing toolKit (Sentry) to generate commands sent from the base station to the sensing nodes. Additional low-level software components are incorporated to control multi-hop communication within a large network, minimize distortion from component noise floor, installation and temperature changes, reduce jitter during sampling, reduce latency of time-synchronized data, and prevent data loss. Figure 3.6 shows block diagrams for the hardware and software architecture of the platform.

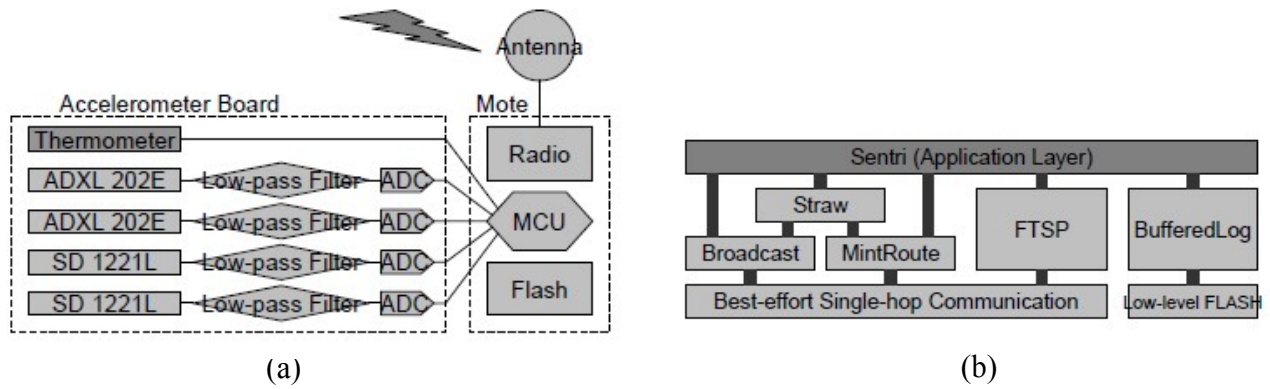


Figure 3.6: (a) Hardware and (b) Software Architecture of Sukun's Sensing Platform.

To validate the system on the field, a 46-hop network was installed on the Golden Gate Bridge in San Francisco (GGB) with the purpose of monitoring structural response to ambient

vibrations and extreme conditions. A total of 64 nodes were mounted along the main span of the bridge and on the southern tower. The base station sends a trigger command and the network samples vibration data at 1 KHz for a period of 12 hours, enough to fill up 512KB of memory on the MicaZ. Although some issues with the routing and synchronizing protocols were encountered, the results of the frequency analysis of the data collected showed clear peaks at frequencies predicted by simulation models.

The authors recognize the reduction of power consumption as a major concern in the design SHM systems. The main source of power for each node is a group of four lantern batteries. At 9V, a node that is idle or sampling data consumes 358.2mW, while a node transmitting data consumer 388.8mW. The most energy expensive operation is erasing flash memory, during which a node consumes a total of 672.3mW. The paper does not provide an estimate for the battery lifetime.

Das *et al.* (1998) introduce the design of a Simultaneous Sensing and Actuating Smart Antenna Element (SSASAE). The basis of the design is a single microstrip antenna distributed on to a piezoelectric substrate connected to digital and analog components. The piezoelectric substrate allows the design to function both as a sensing and an actuating device, making it capable of dynamically stimulating the structure being monitored. The microstrip antenna is made up of a series of patterned narrow metal strips printed on a buried layer of the SSASAE and powered by a remote reader. These strips have the capability to pass electromagnetic waves in either of two polarization directions upon selection. Thanks to this capability, the device can be control with information modulated onto both orthogonal polarization directions of one wireless signal. The device becomes and actuator with information from one polarization orientation, while information from the other polarization orientation request measurement data

from the device acting as a sensor. When performing as a sensor, the device transmits the voltage from the piezoelectric component to a data-acquisition unit by modulating it onto the frequency carrier of the remote reader.

Multiple tests revealed functional prototypes. However, the successful transmission of information occurred only at short distances.

Jung *et al.* (1999) present the development of a wireless sensor based on RFID technology to monitor composite structures. The sensor features a flat loop antenna patterned onto a polymer substrate. The energy from the reader creates an electrical current in the antenna. This current is then stored and used to temporarily power the rest of the circuit. At the core of the sensor unit is a low-power microcontroller and a multiple channel ADC. The ADC receives measurement data from multiple sensors and prepares the information for the microcontroller. The microcontroller then transmits the digital information using amplitude modulation to modulating data onto the carrier frequency of the remote reader.

The unit as a whole consumes a total of 5mW and has a volume of $2.5 \times 2.5 \times 0.3 \text{ cm}^3$. Tests were conducted to study the effects of temperature and pressure on the device embedded in carbon composite plates. The results show that these conditions had no negative impact on the wireless sensor.

Mita and Takahira (2003) propose the design of an RFID based wireless sensor capable of memorizing maximum displacement and strain values of a structural element. The sensor is made of straight thin fluorocarbon wire of 0.291 mm of diameter held by two blocks. While one of the blocks is stationary, the second one is allowed to move along a linear track. When there is displacement in the structure being monitored, the moving block produces a force that exceeds the force of the static friction between the stationary block and the thin wire. This force causes

the wire to slightly pull out of the stationary block. A second force originated from the structural displacement in a direction opposite to the initial displacement will cause the thin wire to buckle elastically, or bend. This distortion represents the memorized value of the peak displacement of the structure under evaluation. This portion of the sensor requires no power supply. Figure 3.7 shows the displacement memorization mechanism.

One of the methods used by Mita and Takahira (2003) to measure the maximum displacement of the gliding block after the distortion occurs involves the use of a capacitor and an inductor connected in series. In this design, one of the blocks made of two coaxial aluminum pipes with a dielectric material in between them acts as a capacitor. The capacitance of the block changes proportionally to the maximum displacement. The change in capacitance causes a change in the frequency of the LC circuit. When the LC circuit is inductively coupled to an RFID reader, the tuned frequency of the wireless communication is directly related to the frequency of the LC circuit. Therefore, any changes in frequency detected by the reader can be translated into the value for maximum displacement measured by the sensor.

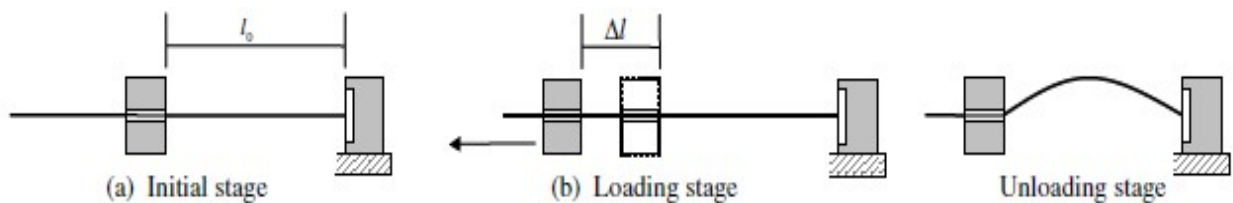


Figure 3.7: RFID-based Strain Sensor.

A laboratory test was set up to verify the operation of the displacement sensor. For this test, the capacitance of the sensor was set to 217pF, giving a resonant frequency of 2.16MHz. The sensor was placed on test equipment capable of producing cycling displacement and the changes in the sensor's resonant frequency were picked up using a dip meter. A high-precision laser displacement sensor was also used to compare measurement data. From the comparison of the

data it was concluded that the RFID based sensor operated properly, accurately reporting peak displacement values.

In order to test the mechanism on the field, the sensor was installed at the base of an isolated-base seven story building on the Keio University campus. The purpose was to measure displacement of isolator plates on the building. Again, the data was compared to simultaneous measurement results from a laser displacement transducer. Similarly to the results from laboratory testing, the measurement results from both sensors on the field were almost identical, with the RFID based sensor having the advantage of maintaining record of the maximum strain after unloading.

Novak *et al.* (2003) present the design of a wireless sensor to monitor civil structures, and more specifically detect two types of damage: cracking in welded steel connections and corrosion in reinforced concrete components. Similar to the design introduced by Mita and Takahira (2002), this sensor utilizes inductive coupling to communicate with a remote reader and the tuned frequency of an LC circuit determines the state of the structure under evaluation.

In addition to the LC circuit, this sensor includes a switch to determine when damage exists in the civil structure. The switch, in both damage detection methods, is implemented with a capacitor of a fixed value initially placed parallel to the capacitor in the LC circuit. When cracking or corrosion occurs, the switch opens, therefore disconnecting the second capacitor from the LC circuit. The change in capacitance of the original circuit results in a change in frequency that is detected by the remote reader.

For the sensor designed to detect cracks, the switch is a copper foil tape that is installed on a welded connection. A 200pf capacitor is placed at the end of the tape, making the total capacitance of the circuit equal to 300pf and a tuned frequency of approximately 8MHz. When a

crack occurs, the tape breaks changing the frequency to 4.8MHz. Tests showed that although the sensing device operates with accuracy, it only reacts to cracks of at least 0.25 inches. Novak *et al.* (2003) found the sensitivity of the device is affected by the quality of the adhesive used on the tape.

For the purposes of corrosion detection the sensor is made of thin steel wire instead. This wire is chosen so that the corrosion rate matches that of the concrete element it is mounted on. When sufficient corrosion takes place the wire breaks, changing the resonant frequency from 8.6 MHz to 6MHz. Simonen *et al.* (2004) and Andringa *et al.* (2004) have both presented the results of tests that verify the effectiveness of the sensing device. Furthermore Andringa *et al.* (2004), have introduced improvements to the hardware of the design that allow the transmission of damage detection data over a distance of 10cm.

Watters *et al.* (2003) introduce the development of the Smart Pebble, a wireless sensor based on RFID technology designed to measure the levels of chloride in concrete bridge decks. The sensor device can be fully embedded into the bridge deck structure thanks to its size, which is similar to that of an aggregate used in the construction of these decks.

The design of the Smart Pebble features a Microchip MCRF202 for wireless communication with a reader. In order to achieve coupling with a remote reader for power and communication, an inductive antenna made up of 300 turns of copper wire around a spool of 2.5 cm in diameter is attached to the MCRF202. The initial frequency of the antenna is set to match the frequency of the communication device at 125 KHz. The proposed sensor to detect chloride levels is a two-electrode electrolytic cell. In the cell, one of the electrodes is set as a reference while the second one is sensitive to chloride ions. With this arrangement, the concentration of chloride ions can be derived from a voltage read by the wireless communication devices.

Furthermore, the design includes a temperature compensation circuit to account for the strong temperature dependence of the sensor.

Results from numerous laboratory tests showed that the wireless sensor is capable of accurately detecting different concentrations of chloride in saturated solutions.

Saafi and Romine (2004) propose the use of a corrosion sensor embedded in concrete structures at the time of construction. The sensor is based on high sensitivity MEMS transducers interfaced with an RFID device for power and communication. The MEMS transducers are designed and fabricated to be capable of detecting changes in pH, relative humidity, chloride concentration levels, as well as CO₂ concentration levels in concrete bridge decks. Polymer films deposited onto a silicon substrate are chemically sensitized to detect changes in each of these parameters. The changes in concentration levels cause the polymer films to expand or contract, therefore changing the resonant frequency of the circuit coupled with the RFID device. The RFID device utilized is a proprietary wireless communication system developed by Microstrain. The reader is designed to interface with sensors embedded 2.5cm below the concrete surface at distances of up to 1.5 cm.

Mascareñas *et al.* (2007) present the design of a novel RFID based “roving-host” wireless sensor network to monitor the health of civil structures. The design is intended to be the basis of an automated monitoring system that quickly provides an assessment of the health of structures and can function for decades without requiring human intervention. In order to accomplish this, the system features the use of an unmanned aerial vehicle (UAV) to power and query individual sensor nodes installed on a structure. The UAV transmits RFID energy to power a sensor node. Upon receiving this energy, the sensor unit acquires a series of measurements and transmits the data back to the UAV, where it is stored in a database for future use. This process is repeated for

multiple sensor units installed in different areas of the structure. An X-cell spectra G helicopter equipped with a computational core, an RF source and 14.5-dBi Yagi antenna, an XBee radio modem, and a wireless camera was used as the UAV in this design.

The core of the sensing unit is a peak displacement sensor known as THINER, designed to operate with very low power. The design of the unit includes an Atmega128L microcontroller, and AD7745 capacitance-to-digital converter, and a Maxtreem XBee radio to allow the sensor to communicate with the UAV and other sensors. Each of these components was carefully chosen to reduce the power consumption of the unit. Moreover, the use of a capacitance-to-digital converter in place of a traditional ADC provides the capability to mechanically acquire and store displacement measurement without a power supply.

The performance of the UAV and sensor nodes is validated on the field at the Alamos Canyon Bridge in New Mexico. The wireless sensing units are placed at the bottom of a support beam along with traditional a tethered sensing system. In addition, a base station is developed to collect and analyze measurement data from both sensing systems, and to control and monitor the RF energy source. As expected, the peak sensor successfully records the maximum strain experienced after a 22-ton dump truck was driven over a 2x4 lumber piece on the bridge. The results from tests to validate the transmission of RF energy show that the UAV is capable of providing enough energy to charge the sensing unit to 3.5V and acquire a series of measurements. The reduction in the amount of power delivered over time, relative to laboratory test results, was attributed to difficulties experienced aligning the antennas.

Chapter 4: Proposed Sensor Prototype for Highway Health Monitoring

This thesis focuses on the development of an ultra-low power sensor designed to be at the core of an extended lifetime highway health monitoring system. The main goal of the design is to accurately measure peak-to-peak displacement on the surface of a road under dynamic traffic loading while operating at very low energy levels.

The following sections offer a description of the architecture of a sensor prototype created to validate the performance of the design, as well as a description of the algorithm developed to obtain displacement figures from acceleration measurements. The final section of this chapter illustrates the process to validate the prototype in a laboratory setting.

4.1 Proposed Architecture of the Sensor Prototype

The proposed architecture of the ultra-low power road health monitoring sensor can be divided into three main components: a sensing device, a computational core, and a communication module. Drawing from previous work discussing the performance of low-cost MEMS in structural health monitoring applications, a dual-axis ADXL202 accelerometer, from Analog Devices, was chosen for this design. An attractive feature of the ADXL202 is the capability of the accelerometer to output a Duty Cycle Modulated (DCM) digital signal. This feature allows any processing core to directly interface with the sensor through a single input pin, thus eliminating the need for an analog to digital converter. The ADXL202 used in this prototype is mounted on a Breakout Board from Sparkfun Electronics. The Digilent Basys board, based on the Xilinx XC3S250E Spartan3E FPGA is selected to perform the functions of the computational core. The capability of this and other FPGAs to achieve concurrent processing make these devices ideal for real-time applications (Chen *et al.* 2007). In order to transmit measurement results to a host computer, a USBMOD4 development module from ELEXOL is included in the

prototype design. A block diagram of the architecture of the sensor prototype is given in Figure 4.1.

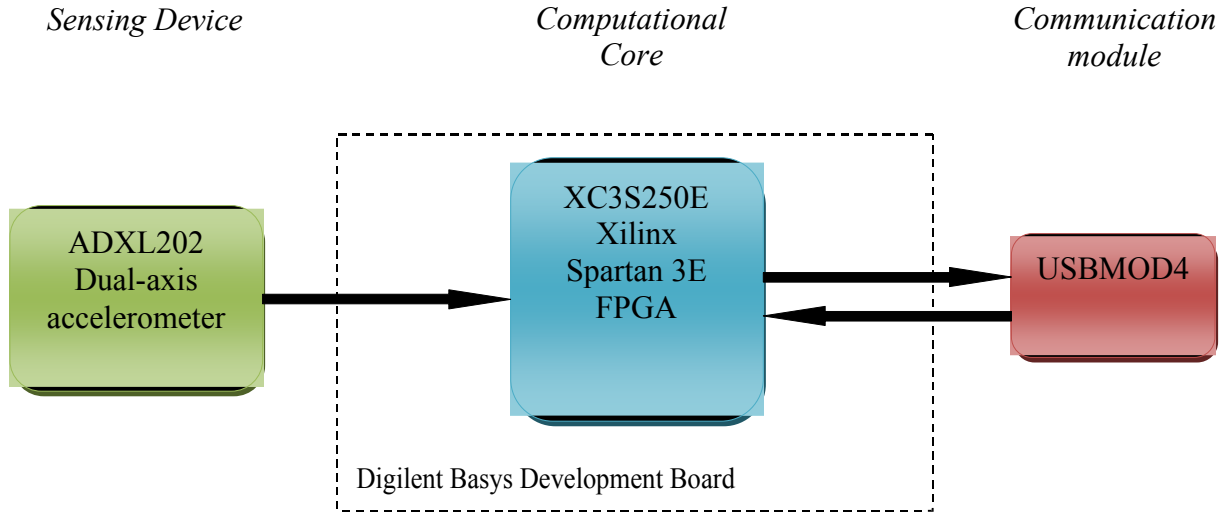


Figure 4.1: Architecture of the Sensor Prototype.

Beyond the requirements for low energy operation of the ultra-low power sensor, the component choices for the computational core and communication module of the prototype were driven by the need to develop a low-cost device to validate the functionality of the ADXL202 and the algorithm to calculate displacement. The Digilent Basys board offers a design platform complete with ready-to-use hardware capable of implementing projects ranging from simple logic designs to complex controller circuits. In addition to the circuitry supporting the operation of the FPGA, the board includes an assortment of on-board I/O devices, as well as four six-pin standard expansion connectors that allow the FPGA to communicate with external components. More importantly, an on-board USB2 port can be used to power the entire board and quickly program the FPGA, without the need for additional power supply or programming cables. The programming interface is designed to work with any of the available Xilinx ISE design tools. An external power supply connector and a JTAG interface are also included. The USBMOD4 is a

single module high-speed USB device based on an FTDI FT245BM Fast Parallel Data Transfer IC. The module can send and receive data at up to 1Mb per second, and it permits the use of Virtual COM port drivers compatible with most of the widely used operating systems. When configured in the USB Bus powered mode, the module does not require an external voltage supply to operate. Moreover, the device is available in a 32-pin Dual In-line Package, making it ideal for prototyping.

4.2 Power Consumption of the Sensor Prototype

The constraint on power consumption is one of the main aspects in the design of the ultra-low power sensor. The purpose of the sensor prototype, however, is to validate the performance of the accelerometer and the algorithm developed to obtain maximum displacement values. Therefore, restrictions on power consumption levels were considered during the selection of components, but without sacrificing the availability of logic capacity and other resources that would make the prototype a flexible and easily reconfigurable device. The issue of significant power consumption reduction is later addressed in the results section of this thesis, in which the layout of an Application Specific Integrated Circuit (ASIC) is presented as an alternative to eliminate the overhead of commercially available microcontrollers and FPGAs.

The power required by the prototype sensor was drawn from the two USB ports incorporated in the design. The Digilent Basys board is powered from the on-board USB port and it delivers a main voltage supply of 3.3V. The board uses supplementary regulators to derive the additional 1.2V and 2.5V supply voltages required by the FPGA. The total current drawn by the FPGA is based upon the logic configuration of the device and the speed of the clock. For this design, the 25MHz clock provided by the on-board oscillator is divided in the firmware to run at 2.5MHz. An estimate of the current drawn when implementing the algorithm to obtain

displacement values at this frequency was acquired with the Xilinx Power Estimator. The USBMOD4 is configured to operate in the USB Bus Powered mode at 3.3V. The 3.3V output pin available on the module is used to power the ADXL202 accelerometer. Table 4.1 provides approximate current and power characteristics of the main components of the sensor prototype.

Table 4.1: Power Characteristic of the Sensor Prototype.

Component	Operating Voltage	Standby Current	Operating Current	Operating Power
ADXL202	3.3 V	0.6 mA	0.6 mA	1.98 mW
XC3S250E (2.5MHz)	VCCINT = 1.2V VCCO = 3.3V VCCAUX = 2.5V			54 mW
USBMOD4	3.3 V	100 μ A	25 mA	82.5 mW
Total				138.48 mW

These values are compared to the power consumption figures of the ASIC layout presented in the results section of the paper.

4.3 Design Parameters for the ADXL202

The design procedure when using the ADXL202 requires the selection of components to determine the period of the DCM output, as well as the bandwidth of the accelerometer. The resolution and the noise characteristics of the device are dependent on the value of these parameters.

4.3.1 Setting the Bandwidth of the ADXL202

The bandwidth of the ADXL202 accelerometer can be adjusted with external capacitors CX and CY. These capacitors must be connected to the corresponding XFILT and YFILT pins of the accelerometer in order to implement low-pass filtering to reduce noise and prevent aliasing. Table 4.2 provides a range of bandwidth values available with the ADXL202 and the associated values of capacitors CX and CY.

The accelerometer bandwidth for this design was set at 50 Hz to allow for the detection of traffic induced vibrations on roads with different levels of fatigue. The predominant frequencies of vibrations produced by road traffic are in the range of 5 to 25Hz, and the amplitudes are typically between 0.005 and 0.2g's of acceleration (Hunaidi 2000). The motion of a typical 5-axle semi-trailer driving at highway speeds produces ground vibrations with dominant frequencies in the range of 10 to 15 Hz. As the pavement surfaces are never completely smooth and there always dynamic components to a moving vehicle, the dynamic force exerted on the ground by the tires is usually 15% higher than the corresponding static force. As a result, random ground vibrations are always present. Specific pavement irregularities, however, can increase this dynamic force by up to 50 to 80 % in comparison to the static force. An increase in ground vibrations is proportional to this increment in the value of the dynamic force (Hajek 2006).

Table 4.2: Filter Capacitor Selection Cx, Cy.

Bandwidth	Capacitor Value
10 Hz	0.47 μ F
50 Hz	0.01 μ F
100 Hz	0.05 μ F
200 Hz	0.027 μ F
500 Hz	0.01 μ F
5 kHz	0.001 μ F

According to the specifications provided by the manufacturers of the ADXL202, the typical noise floor of the accelerometer can be found using equation 5.

$$Noise(rms) = \left(200 \frac{\mu g}{\sqrt{Hz}}\right) * (\sqrt{BW * 1.6}) \quad (5)$$

At 50 Hz, the noise is

$$Noise(rms) = \left(200 \frac{\mu g}{\sqrt{Hz}}\right) * (\sqrt{50 * 1.6}) = 1.79mg \quad (6)$$

The peak-to-peak noise values can be estimated by statistical methods. Table 4.3 shows characteristic noise outputs for the ADXL202 provided by Analog Devices.

Table 4.3: Typical Noise Output for the ADXL202.

Bandwidth	CX, CY	rms Noise	Peak-to-Peak Noise Estimate 95% probability (rms x 4)
10 Hz	0.47 μ F	0.8 mg	3.2 mg
50 Hz	0.1 μ F	1.8 mg	7.2 mg
100 Hz	0.05 μ F	2.5mg	10.1mg
200 Hz	0.027 μ F	3.6 mg	14.3 mg
500 Hz	0.01 μ F	5.7 mg	22.6 mg

Conveniently, the Breakout Board from Sparkfun Electronics used in the design of the sensor prototype comes fully assembled with 0.1 μ F filtering capacitors.

4.3.2 Setting and decoding the DCM output

As part of the design process, the ADXL202 is calibrated to determine the duty cycle of the output and the sensitivity of the device operating at 3.3V. The nominal duty cycle output of the ADXL202 (5V) is 50% at 0g with a 12.5% duty cycle change per g of gravity detected. The value for acceleration can be decoded from the DCM output with equation 7, where $T1$ is the length of the “on” portion of the cycle and $T2$ is the length of the period (fig 4.2).

$$Acceleration (g) = \frac{\left(\frac{T_1}{T_2}\right) - 50\%}{12.5\%} \quad (7)$$

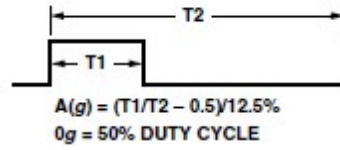


Figure 4.2: DCM Output from the ADXL202

In order to determine the sensitivity of the accelerometer at 3.3V, a calibration method using the duty cycle values measured at the +1g and -1g positions is carried out. The value of the duty cycle with the x-axis pointing in the direction of the force of gravity was measured at 38.46%, while the measurement with the x-axis pointed in the opposite direction yielded a 61.73% duty cycle. The sensitivity of the accelerometer is calculated using equation 8.

$$\text{Sensitivity} = \frac{61.73\% - 38.46\%}{2g} = 11.635\% \text{ per } g \quad (8)$$

Because the monitoring sensor is designed to detect acceleration and displacement along the z-axis, the value for the duty cycle at 0g is adjusted to account for the force of gravity. In order to measure displacement along the z-axis, the ADXL202 is oriented with the x-axis pointing in the direction of the force of gravity (fig. 4.3). At this position, the duty cycle of the output is 38.46%; therefore, the formula to decode the DCM output used in this design is given by equation 9.

$$\text{Acceleration } (g) = \frac{\left(\frac{T_1}{T_2}\right) - 38.46\%}{11.635\%} \quad (9)$$

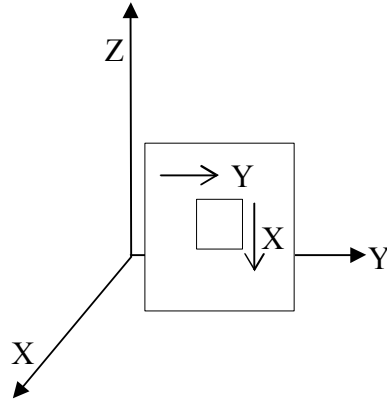


Figure 4.3: Orientation of the ADXL202.

Given that one of the requirements for the monitoring sensor is the acquisition of data within a time frame of about one second, the period of the DCM output is set at 1 ms. This value allows for the collection of 1000 acceleration data points to be used in the algorithm to obtain peak-to-peak displacement numbers. The period of the DCM output signal of the ADXL202 can be set anywhere from 0.5 to 10 ms using a resistor connected between the RSET pin and ground. Equation 10 describes the relationship between the resistance RSET and the period of the output.

$$T2 = \frac{R_{SET}(\Omega)}{125M\Omega} \quad (10)$$

In this case, a 1MOhm resistor included on the Breakout Board is replaced with a 127KOhm resistor.

The resolution of the acceleration measurements is limited by the speed of the device used to decode the DCM output. The selection of the speed of the counter used to decode the output was a tradeoff involving the need for a resolution that would allow the detection of acceleration amplitudes in the order of 5 mg, and the reduction of power consumption of the FPGA. The result is the use of a clock running at 2.5 MHz. At this frequency and with a measured $T2$ period of 1.03 ms, the count value for a whole period is approximately 2575. The resolution of the accelerometer is then given by equation 11.

$$Resolution (mg) = \frac{1}{count\ per\ g} \times 1000 \quad (11)$$

$$Resolution (mg) = \frac{1}{0.116 \times 2575} \times 1000 \approx 3mg \quad (12)$$

It is important to note that this is the resolution given only by the counter used to decode the DCM output. The lower limit of the resolution is also determined by the noise characteristics of the ADXL202.

4.3 Double Integration Algorithm

The approach taken to obtain peak-to-peak displacement information from acceleration data is driven by the requirement to significantly reduce the power consumption of the sensor. The algorithm is based on the definition of acceleration as

$$a(t) = \frac{d^2 x}{dt^2} \quad (13)$$

where x represents the distance traveled during a time interval t . This definition implies that a value for displacement can be obtained by integrating acceleration data twice over a determined period of time. The two approaches to numerically integrate a signal involve the analysis of data in the frequency or the time domain. While analyzing acceleration information in the frequency domain has many benefits, for SHM applications in particular, the implementation of a Fast Fourier Transform (FFT) algorithm to convert data to the frequency domain can be computationally expensive. Given that the requirements for the monitoring sensor are limited to the acquisition of displacement information to evaluate the integrity of a road, a simpler

algorithm based on the rectangular rule for numerical integration is applied to integrate acceleration data twice in the time domain.

The rectangular rule for numerical integration shows that for any random function $X = f(t)$, the area under the curve can be found with equation 14.

$$S = \int_{T_0}^{T_1} f(t) dt \quad (14)$$

Furthermore, if the area between T_1 and T_0 can be divided into small enough intervals Δt (fig 4.4), the integral of $X = f(t)$ can be approximated with the sum of an n number of rectangles.

$$S = \sum_{i=0}^{n-1} X_i \Delta t = \Delta t \sum_{i=0}^{n-1} X_i \quad (15)$$

$$v = \Delta t \sum_{i=0}^{n-1} a(t)_i \quad (16)$$

$$x = \Delta t \sum_{i=0}^{n-1} v(t)_i \quad (17)$$

From this principle, displacement x can be found with equation 18, where it is assumed that the accelerometer is initially at rest and acceleration and displacement are equal to zero.

$$x = \Delta t^2 \sum_{i=0}^{n-1} v(t)_i + a(t)_{i+1} \quad (18)$$

The application of this method for numerical integration translates the task of obtaining displacement values from acceleration data into two basic operations, accumulation and multiplication (Chen *et al.* 2007).

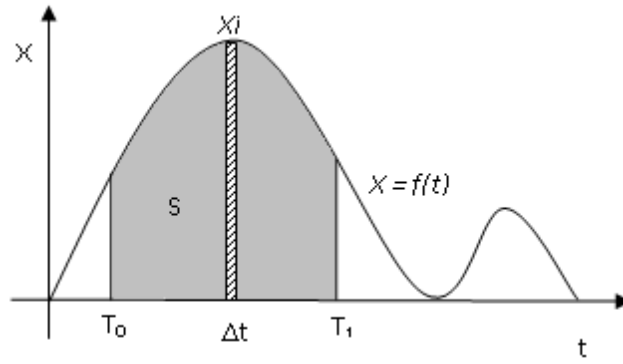


Figure 4.4: Integral of $X = f(t)$ from T_0 to T_1 .

Making use of the functional flexibility of FPGAs, an algorithm to accumulate samples proportional to acceleration is developed for the Xilinx XC3S250E using Verilog Hardware Description Language. A flow diagram summarizing the accumulation procedure is given in Figure 4.5. As shown in the diagram, the Verilog program uses a counter to measure the length of pulse $T1$. This counter is started at the rising edge of the DCM output from the accelerometer, and it is incremented while this signal is high. At the falling edge of the input pulse, the value is saved onto register $T1$ and used to calculate a value proportional to acceleration stored in register ACCEL. The counter is cleared before the next DCM pulse is encountered. Every time a new value proportional to acceleration is computed, the value is added to accumulator VEL to obtain velocity, and the new value in VEL is added to accumulator DISP to obtain displacement as described in equation 18. The program uses registers MIN_DISP and MAX_DISP and a comparator to keep track of the maximum and minimum displacement values reached after every accumulation cycle. A second counter incremented only at the rising edge of the DCM output is used to determine when one second has elapsed. Once this timer reaches 1000, a peak-to-peak displacement value is found by adding the contents of the registers holding the maximum and minimum values, the 24-bit result is written to the USBMOD4, and the registers are cleared. The final output of the Verilog algorithm is a 24-bit figure proportional to displacement.

These displacement data points are later multiplied by the appropriate constants using Matlab to complete the integration process. Since the amount of current drawn by the FPGA is dependent upon the logic configuration of the device, relegating all multiplication operations to a host computer will further minimize the power consumption of the computational core of the sensor. The first coefficient taken out of the double integration algorithm corresponds to the formula to decode the DCM output of the accelerometer. Rearranging equation 5 to express acceleration as a difference, equation 19 is as follows.

$$(T2) \times (11.635\%) * Acceleration (g) = T1 - T2 \times 38.46\% \quad (19)$$

Seeing as period $T2$ remains constant, the value subtracted from $T1$ in the firmware is

$$2575 \times 0.3846 \approx 990$$

Therefore, the output of the accumulation process performed by the FPGA has to be multiplied once by

$$\frac{1}{2575 \times 0.1163} \approx 0.00334$$

The product of this operation must be then multiplied twice by Δt^2 as given in equation 18. If every sample in the integration procedure corresponds to a DCM output with a 1 ms period, then $\Delta t = 0.001$ seconds. A third and final coefficient must be used to express the displacement values in inches. Since the formula to decode the DCM output of the ADXL202 yields acceleration in g's, and $1g = 386.088583$ inches, the output from the FPGA must be multiplied by this conversion factor.

In brief, the output from the FPGA is converted to values corresponding to peak-to-peak displacement in inches for a given set of acceleration data using equation 20.

$$Pk - Pk Displacement (in) = (0.00334) \times 0.001^2 \times 386 \times FPGA Output \quad (20)$$

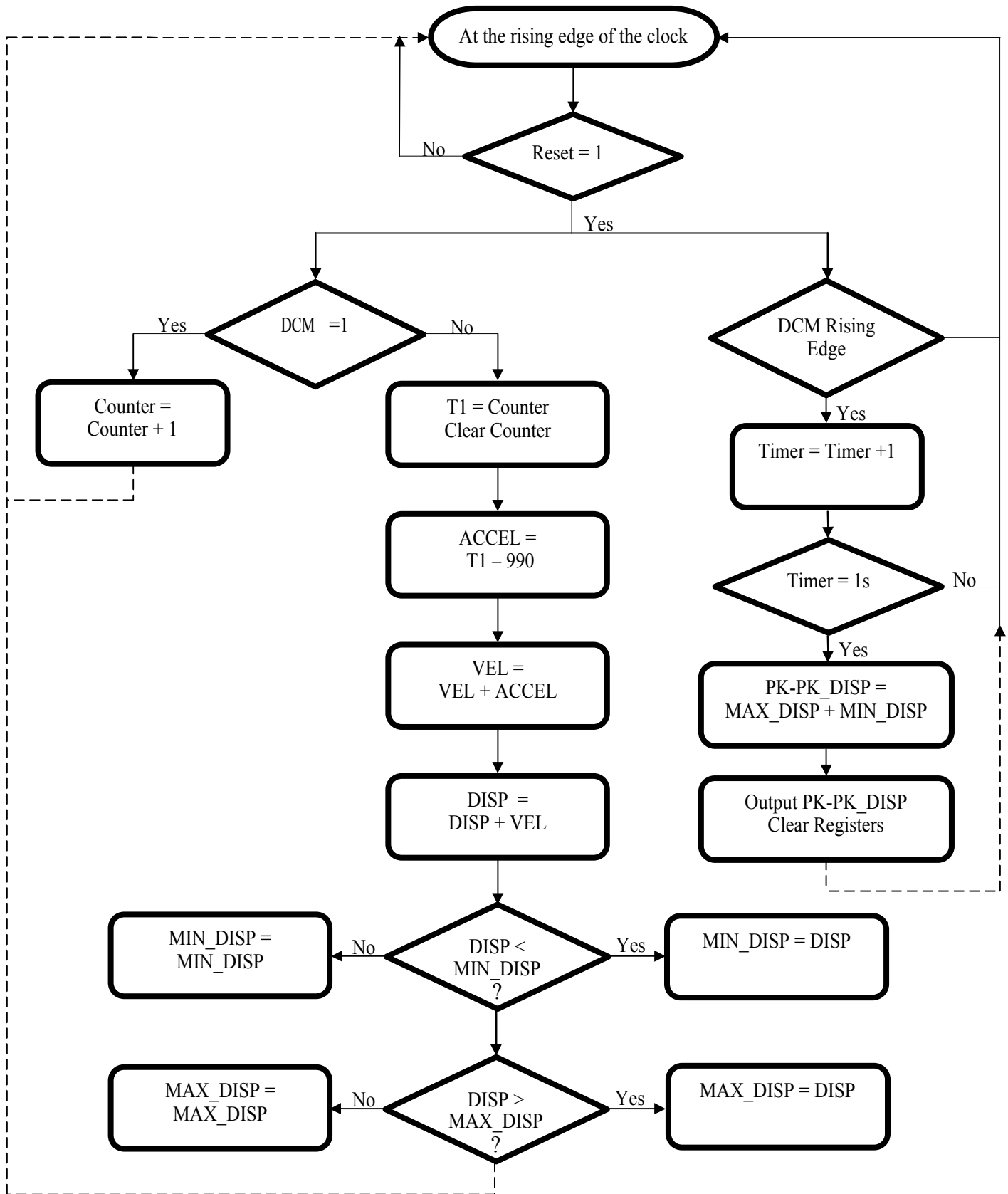


Figure 4.5: Verilog Algorithm to Perform Accumulation.

4.4 Sensor Prototype Validation

The overall performance of the completed sensor prototype is validated in a controlled laboratory setting. During a preliminary test procedure, data is collected corresponding to the measured values of pulse TI with the accelerometer placed on a flat surface and oriented in three different directions: parallel to the ground, with the x-axis pointing in the direction of the force of gravity, and with the x-axis pointing in the opposite direction of the force of gravity. These positions correspond to the nominal 0g, +1g, and -1g durations of the TI pulse. The purpose of this test is to verify the resolution of the accelerometer against the information obtained in the design procedure.

A second test is used to validate the performance of the accelerometer and the double integration algorithm in response to sinusoidal excitation. In particular, this validation procedure is used to verify that the sensor prototype can accurately detect 0.02 inches of displacement. According to information relayed by Dr. Soheil Nazarian, a displacement of this magnitude on a road under dynamic traffic loading is indicative of pavement fatigue. For this purpose, the sensor prototype is placed on the surface of a single axis EA1500 shaker from MB Dynamics. This shaker vibrates along the z-axis and can produce accelerations of up to 124 g's and a force vector of up to 50 lbs. The shaker is driven with a Labworks Inc. CP-123 Power Amplifier receiving signals generated on a PC using Virtual Bench. The signals used to test the prototype are sinusoids with frequencies ranging from 1 to 30 Hz. Displacement measurements from a 5mm Bently Nevada 7200 proximator mounted alongside the sensor prototype are used as a reference. The amplitude of the driving sinusoids is adjusted every time the frequency is changed to maintain the signal coming from the proximator at a constant peak to peak voltage of 1.6 V. According to the calibration factor for the reference device, this voltage is proportional to

approximately 0.02 inches of displacement on the shaker. For each frequency tested, displacement data from the sensor prototype is collected for a period of 90 seconds with a laptop using Hyper Terminal. The Hyper Terminal characters are later converted to hexadecimal and decimal equivalents and are processed with MATLAB. Figures 4.6 and 4.7 demonstrate the laboratory validation setting.



Figure 4.6: Laboratory Validation Setting.

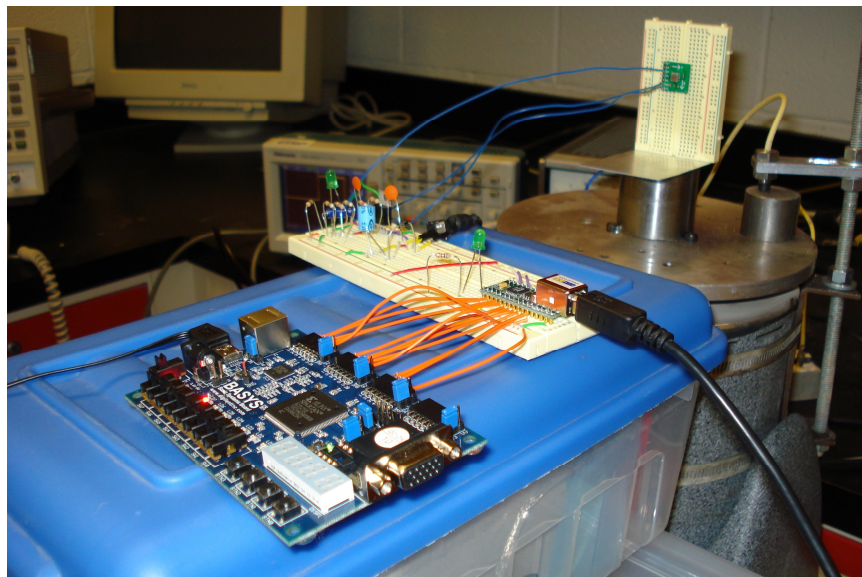


Figure 4.7: Sensor Prototype in the Laboratory Validation Setting.

In order to better understand the results from this testing procedure, key concepts regarding the behavior of sine vibration are reviewed.

4.5 Sine Vibration Testing

When inducing or measuring sine vibration, it is important to consider how the phase and magnitude of acceleration, velocity, and displacement are related. For sinusoidal vibration, acceleration leads velocity by 90° and displacement by 180° as shown in Figure 4.8 (Goldman 1999). The relationship between the magnitude of acceleration, velocity, and displacement is directly proportional and frequency dependent (Labworks Inc 2009). At a particular frequency, the values of acceleration, velocity and displacement are related by a single proportionality constant. This proportionality constant changes if the frequency of the vibration is changed. Consequently, the values for all parameters of sine vibration can be found for a given frequency if at least one of these parameters is known. The relationship between acceleration, velocity and displacement for sinusoidal vibration is expressed in equations 21 through 23 where f is the frequency of the vibration, g is equal to peak acceleration in g's, V represents peak velocity in inches per second, and D is equal to the peak-to-peak displacement in inches.

$$g = 0.0511f^2D \quad (21)$$

$$g = 0.0163Vf \quad (22)$$

$$V = \pi fD \quad (23)$$

The equations for each of these parameters are directly obtained from the sinusoidal function resulting from analytical integration of the corresponding parameter evaluated at the peak value.

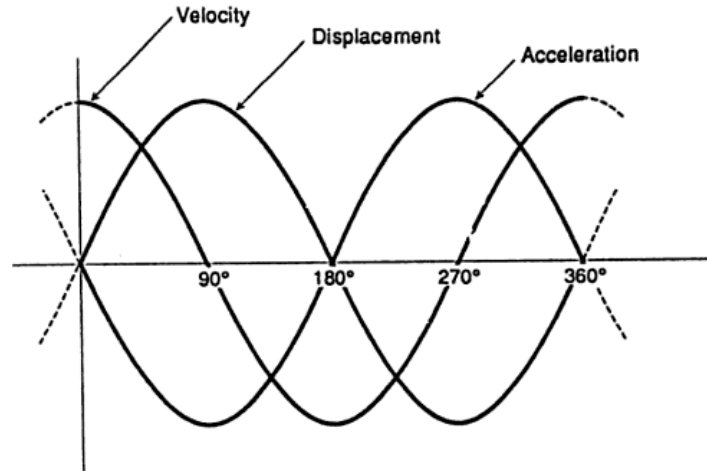


Figure 4.8: Phase Relation of Acceleration, Velocity, and Displacement.

Since displacement and frequency values are known for the testing procedure, the expected peak values of acceleration and velocity for each of the signals used to drive the shaker can be found. Table 4.4 shows the peak acceleration and peak velocity values at each frequency tested for a corresponding peak to peak displacement of 0.02 inches.

Table 4.4: Parameter Values for Sinusoid Vibration Testing.

Frequency	Acceleration (g's)	Velocity (in/s)	Displacement (in)
1 Hz	0.0010	0.06283	0.02
5 Hz	0.0256	0.3142	0.02
10 Hz	0.1022	0.6283	0.02
15 Hz	0.2301	0.9425	0.02
20 Hz	0.4088	1.2566	0.02
25 Hz	0.6388	1.5708	0.02
30 Hz	0.9198	1.8850	0.02

Chapter 5: Results

5.1 Experimental Results

The results of the preliminary tests to validate the resolution of the accelerometer showed that there is some fluctuation in the value of pulse $T1$ due to noise and temperature. The values obtained from monitoring the length of the $T1$ pulse at the 0g, +1g, and -1g positions showed that this length varies by up to a unit when the accelerometer is at rest. This fluctuation is attributed to the noise characteristics of the ADXL202 and it is apparent when the DCM output is observed on an oscilloscope with a time per division in the order of hundreds of nanoseconds. Since the period of the clock used to monitor the $T1$ pulse is 400 ns, this fluctuation is caught by the counter. Although the occasional difference between the constant for $T1$ at rest used in the algorithm and the actual $T1$ measured is negligible in terms of acceleration, this discrepancy grows quickly when added by the accumulators over one second. Therefore, the accumulation of this difference results in relatively large numbers for displacement when the accelerometer is motionless. As expected, the effects of the noise floor of the ADXL202 have a significant impact in the displacement results for sinusoid vibration at frequencies below 3 Hz, where peak acceleration is less than 1.79 mg. Furthermore, it is important to note that the length of pulse $T1$ and period $T2$ are temperature dependent and the accelerometer needs to be recalibrated periodically in order to update the constants used in the algorithm.

The output values obtained after a first round of testing on the shaker showed that 0.02 inches of peak-to-peak displacement cannot be found using only the numerical integration algorithm and coefficients described previously because of the nature of sinusoid vibration and the lack of information about the initial state of all vibration components. In order to verify the results obtained with the prototype, the same numerical double integration algorithm is

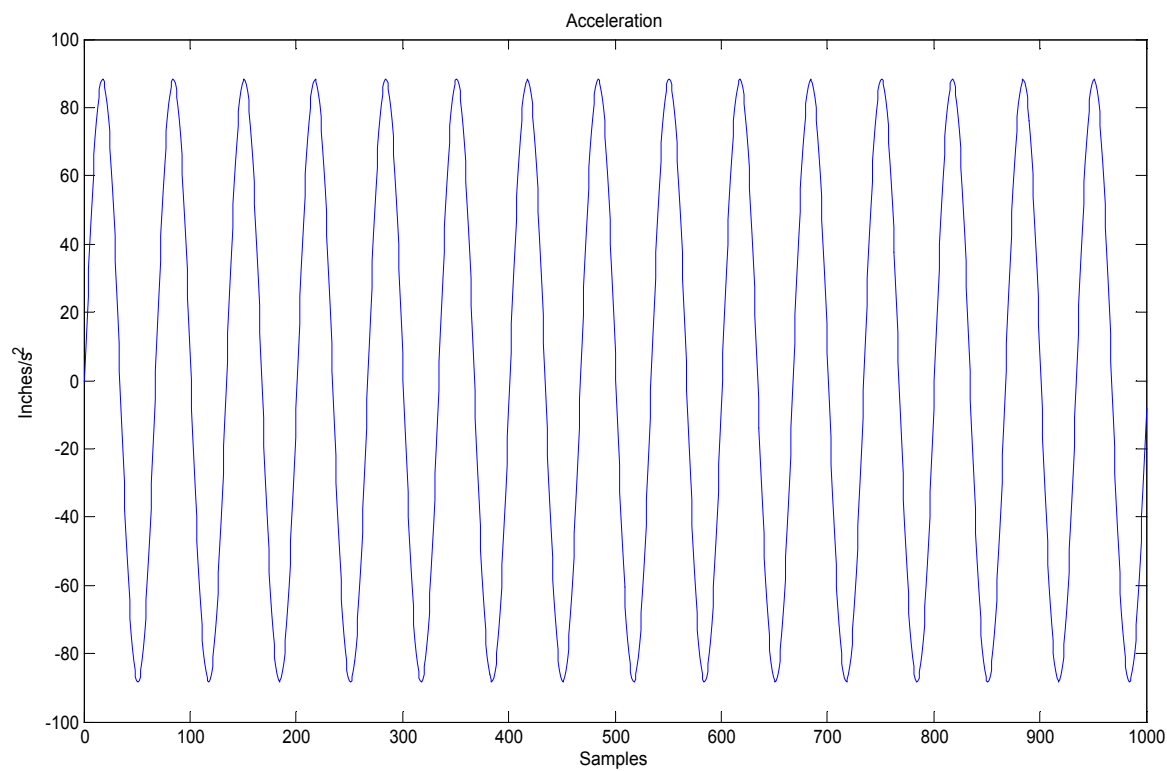
implemented in Matlab for a sinusoid representing acceleration with peak amplitude of 88.8 in/s^2 (0.223 g's) and a frequency of 15 Hz. These acceleration specifications correspond to a peak-to-peak displacement of 0.02 inches. For further verification, the cumulative trapezoid integration function was applied to the same sinusoid and compared to the results of the rectangular integration algorithm. The results from applying both numerical integration algorithms to 1000 points with 0.001 spacing and starting at zero revealed that the accumulation process produces a velocity sinusoid that oscillates above zero and a displacement curve that grows to large positive values (fig 4.9). Moreover, the maximum values obtained after double integration did not correspond to peak-to-peak displacement. Instead, the plot shows that the maximum value reached after the second integration corresponds to the peak velocity associated with the peak acceleration of the original sinusoid. From Figure 4.9c, the maximum value reached is 9.358×10^5 . This value multiplied by $\Delta t^2 = 0.000001$ corresponds to the peak velocity in inches shown in Table 4.4 for a 15 Hz signal. This effect was attributed to the absence of an initial condition in the numerical integration algorithm and the accumulation of the error caused by the lack of this offset. From the phase relation between sinusoid vibration parameters (fig. 4.8) is it evident that velocity is at the highest value when acceleration and displacement are zero. Since the numerical integration algorithms in Matlab were applied to a sinusoid starting at 0, an additional offset value is needed in the double integration procedure to account for the initial conditions of all sinusoid vibration components.

After analyzing Matlab results for multiple sinusoid acceleration signals, a coefficient equal to the inverse product of π times the frequency of acceleration is chosen to account for the initial condition of the vibration components. Matlab results for sinusoids at each of the frequencies of interest are consistent with those obtained for a 15 Hz acceleration signal. In every

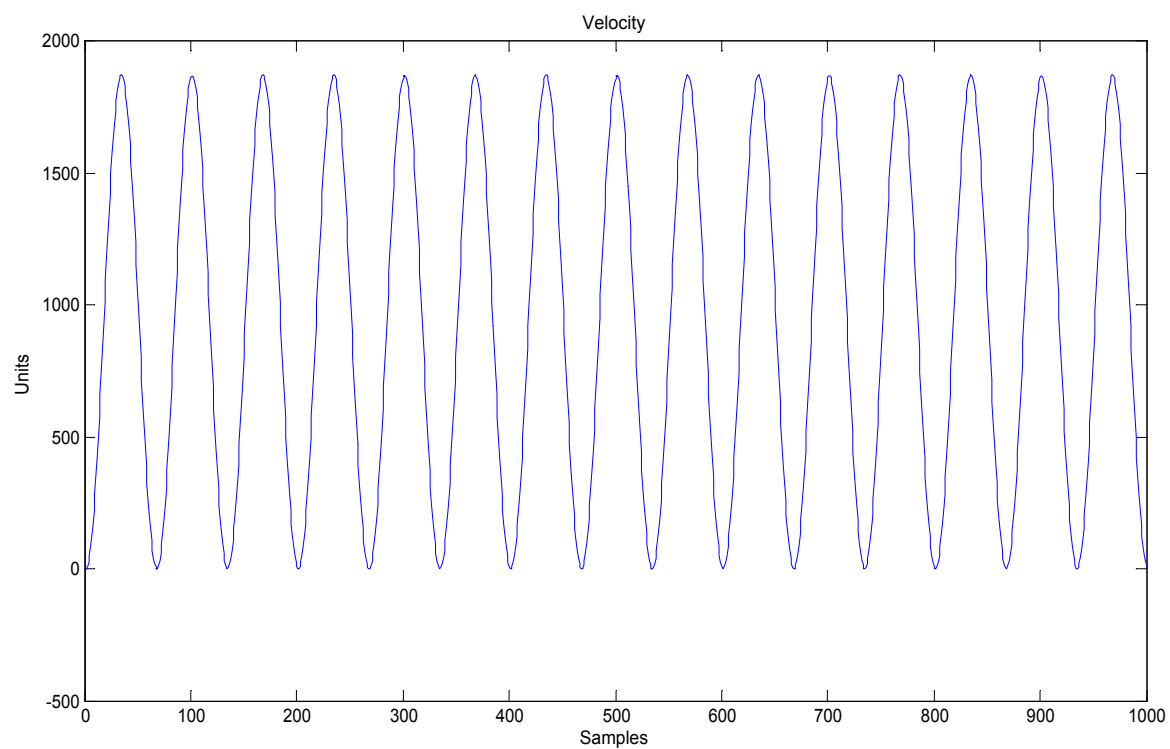
case, the value obtained from double numerical integration of 1000 points starting at 0 was proportional to peak velocity. Based on equation 23, the value for displacement can be found by dividing velocity over π times the frequency of vibration (24).

$$D \text{ (inches)} = \frac{0.9358}{15 \times \pi} = 0.019916 \quad (24)$$

Further exploration of sinusoid vibration in Matlab revealed that the output of the numerical integration algorithm, as described in section 4.3, is equal to peak-to-peak displacement only when the sinusoid is integrated over exactly one period and taking the maximum or minimum acceleration value as the starting point. Figure 4.10 shows the plots corresponding to the integration over one period of the 15 Hz acceleration signal.



(a)



(b)

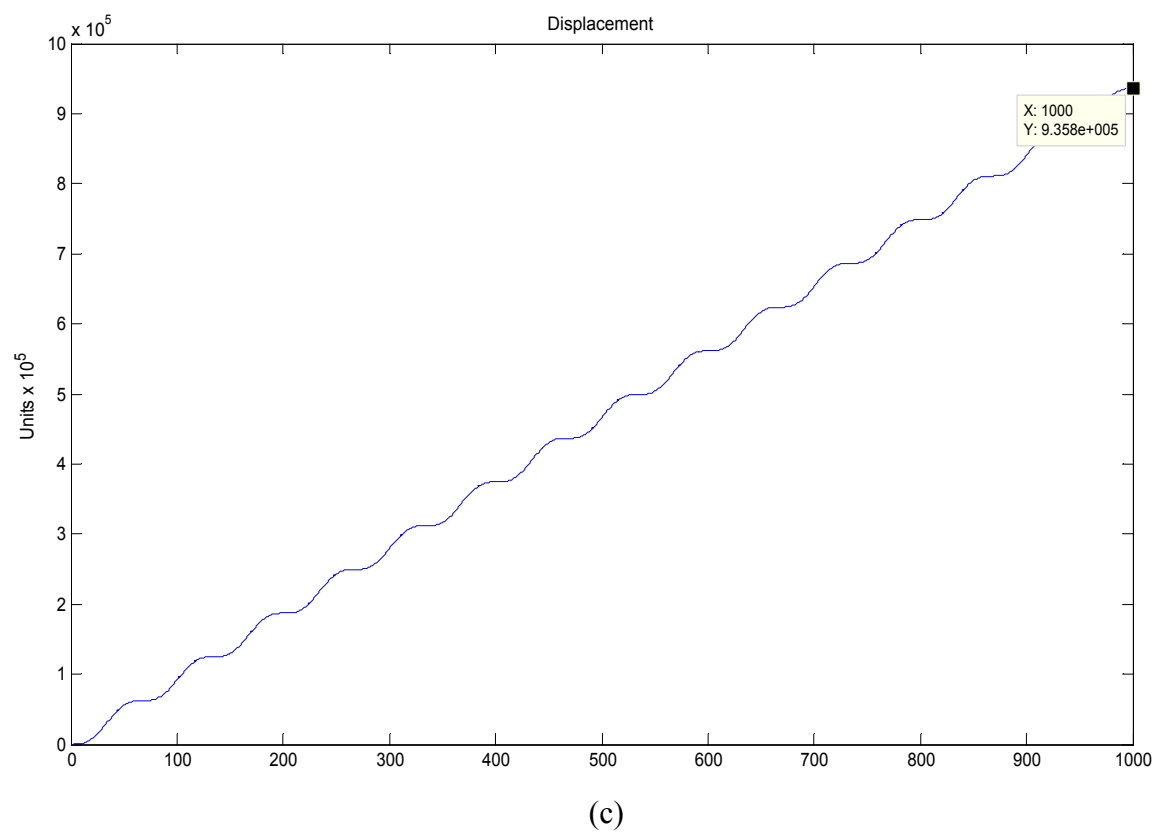
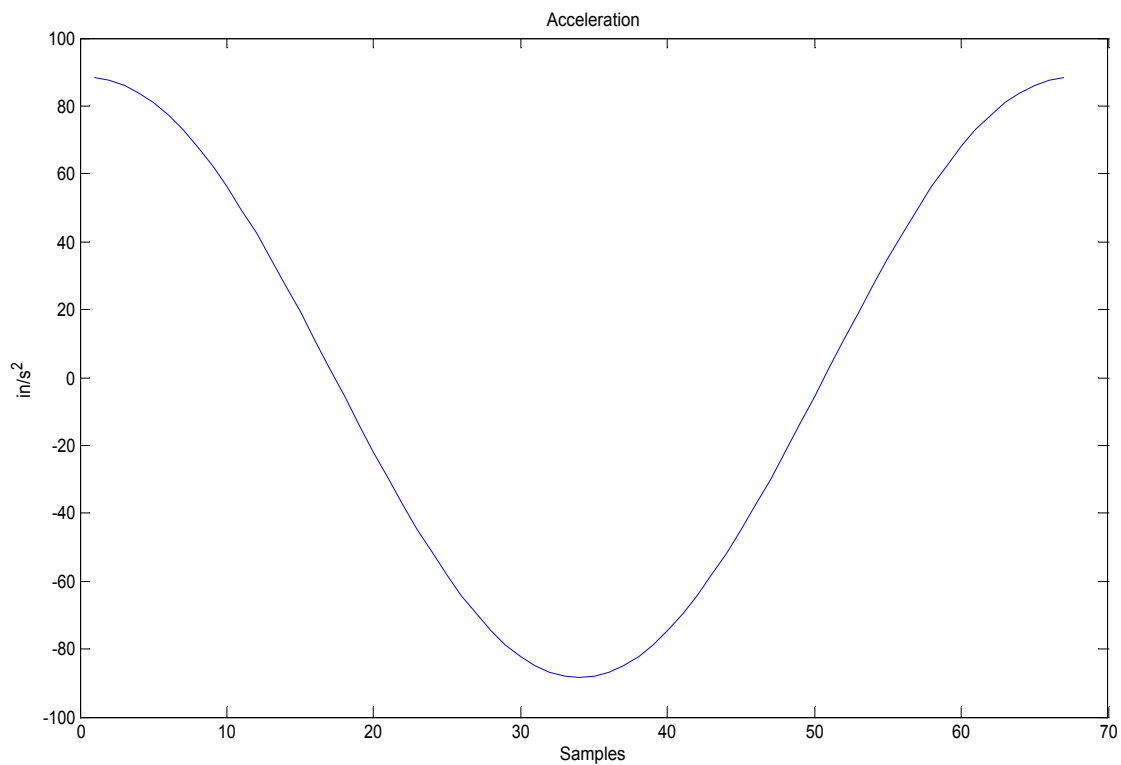
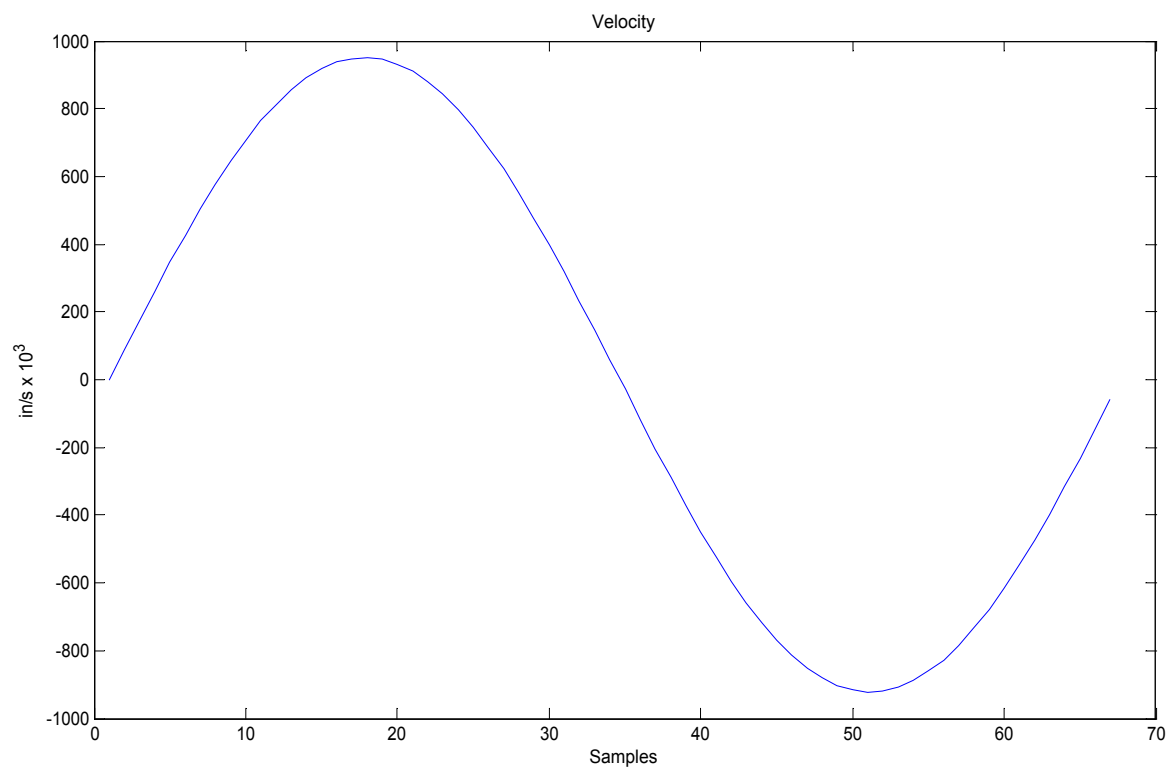


Figure 5.1: (a) Acceleration (b) Velocity Lacking Initial Condition Offset After First Accumulation and (c) Accrued Initial-condition Error after Second Accumulation.



(a)



(b)

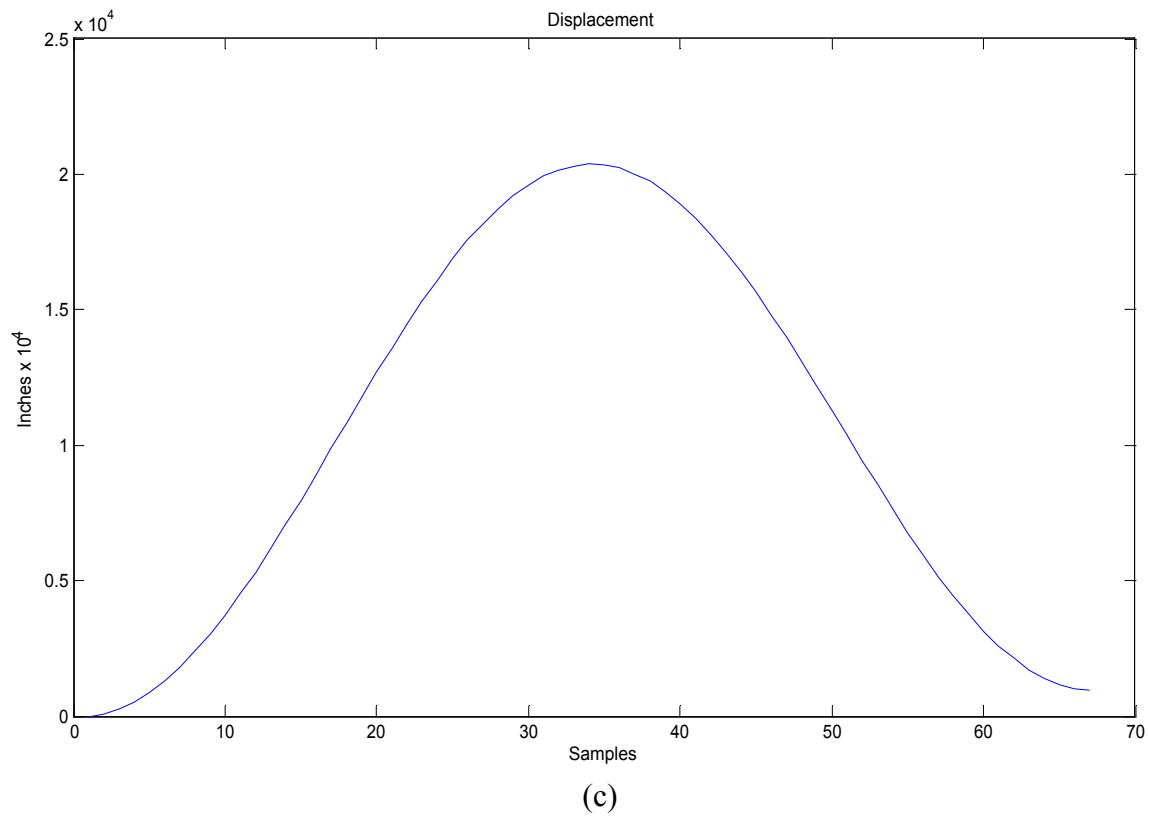
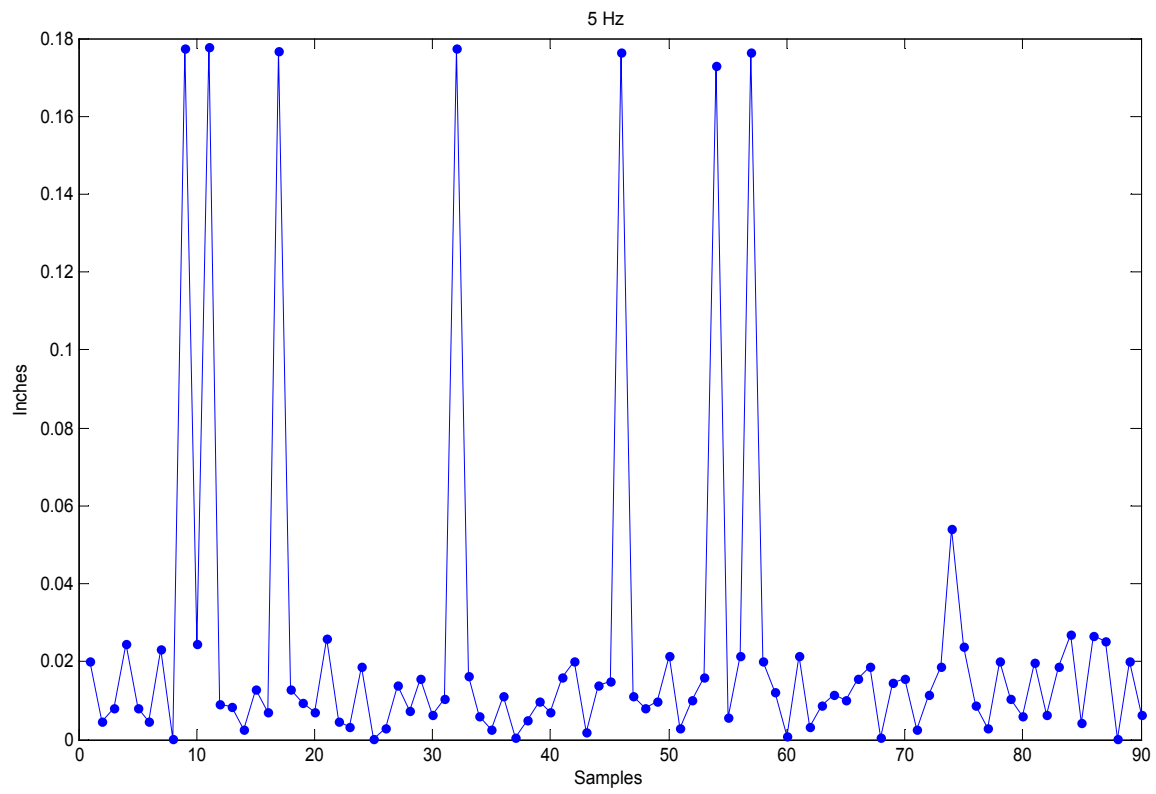


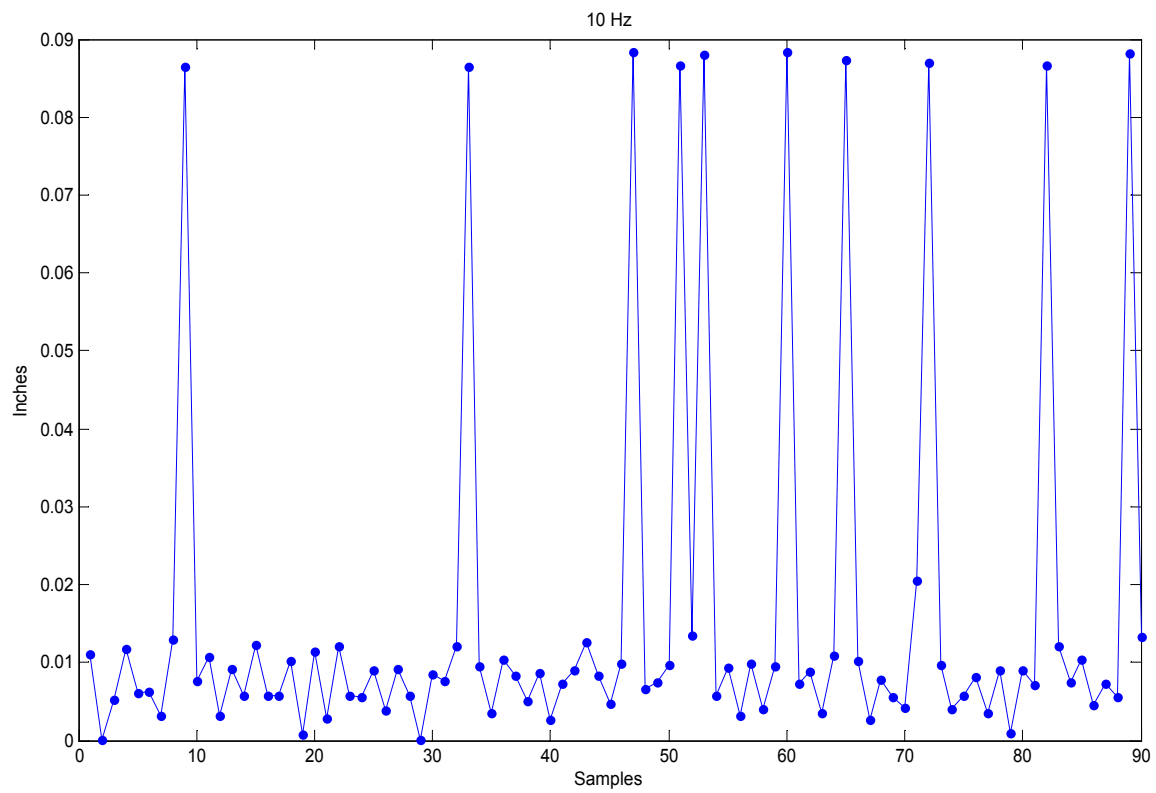
Figure 5.2: 15 Hz (a) Acceleration (b) Velocity and (c) Displacement over One Period.

Based on the conclusions drawn from the Matlab analysis, the prototype was placed on the shaker again and the output was multiplied by a fourth coefficient equal to $1/(f\pi)$. The result was displacement in inches with maximum values very close to the target 0.02 inches. The data obtained over 90 seconds for each frequency of interest is presented in Figures 4.11 and 4.12. With the exception of a few high peaks, the plots for displacement at frequencies between 5 and 30 Hz show that the maximum displacement measured corresponds to values between 0.015 and 0.02 inches. The need to adjust the amplitude of the driving signal for each frequency, and the acquisition speed of the Virtual Bench oscilloscope are factors that prevented from having a constant displacement of exactly 0.02 inches on the shaker. Therefore, the maximum output from the prototype is slightly higher or lower than 0.02 inches and somewhat different for each frequency. Peaks exceeding 0.02 inches and very low values are attributed to errors in the

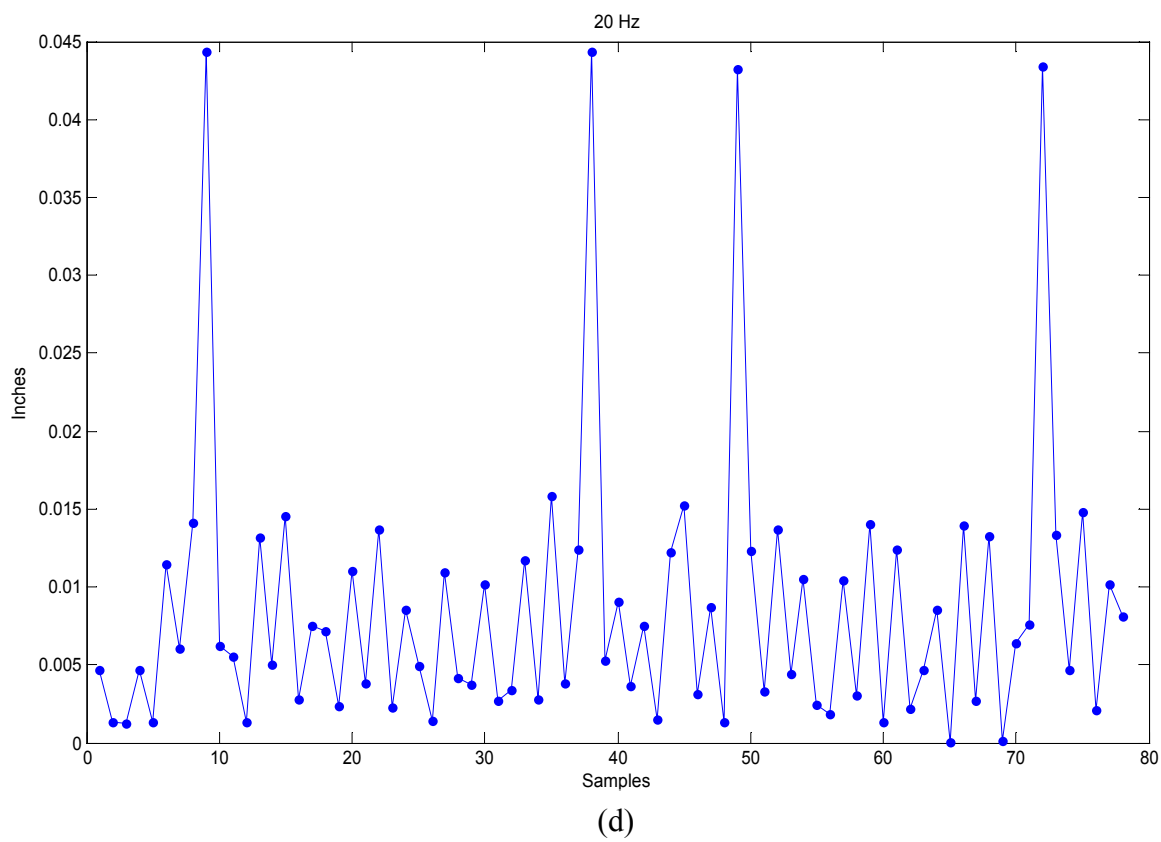
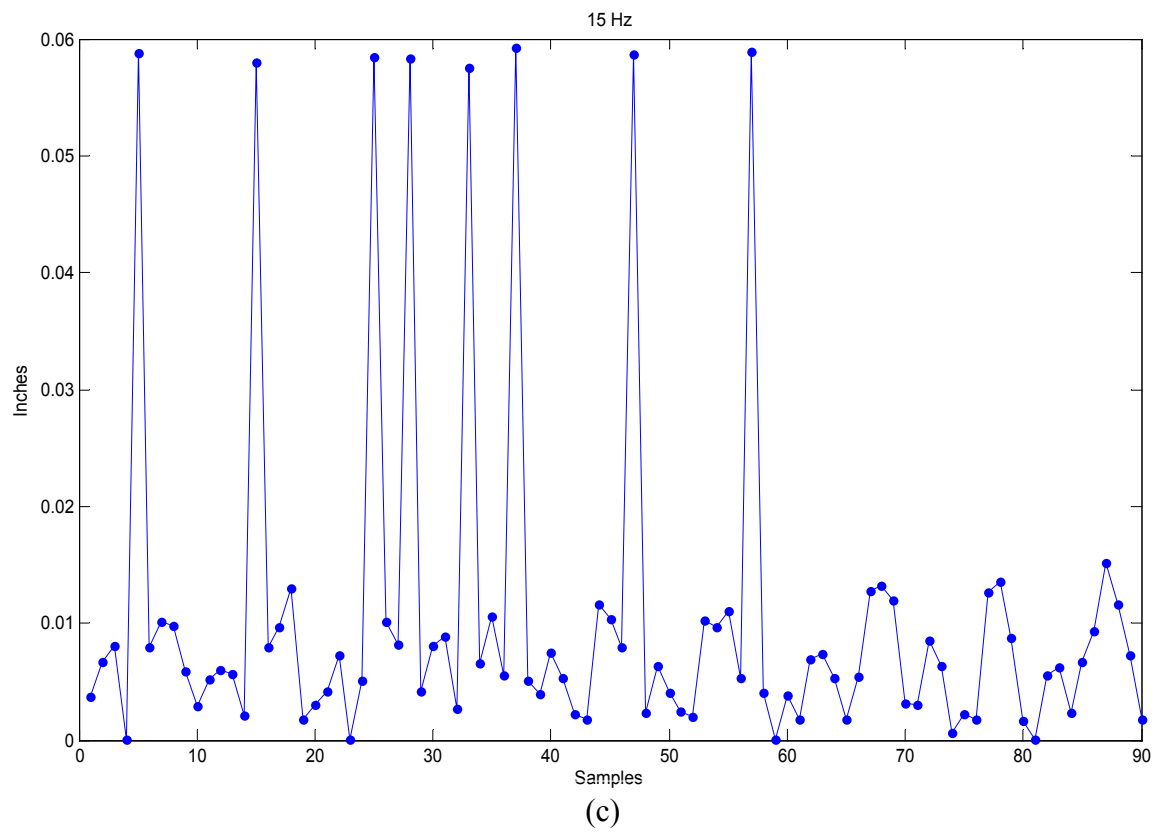
translation from Hyper Terminal characters to hexadecimal and decimal equivalents. 8-bit values corresponding to and end of text, carriage return, or a new line characters in ASCII code were taken by a conversion script as null or bytes equal to 32h. This conversion error resulted in incorrect values when the 24-bit output is converted to decimal. Removing the high peaks caused by translation errors from the 1 Hz signal plot (fig. 4.12b) it is evident that the noise floor of the ADXL202 has an effect in the accumulation of error and the production of outputs greater than 0.02 inches.



(a)



(b)



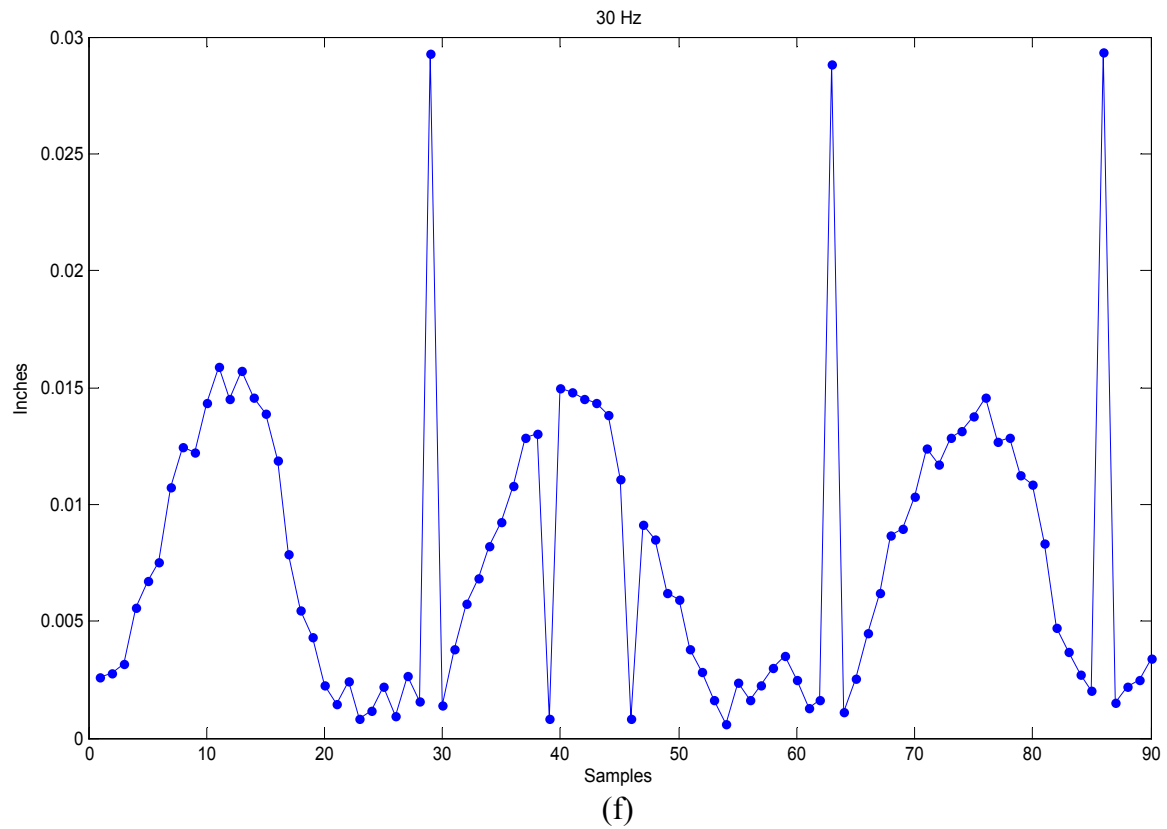
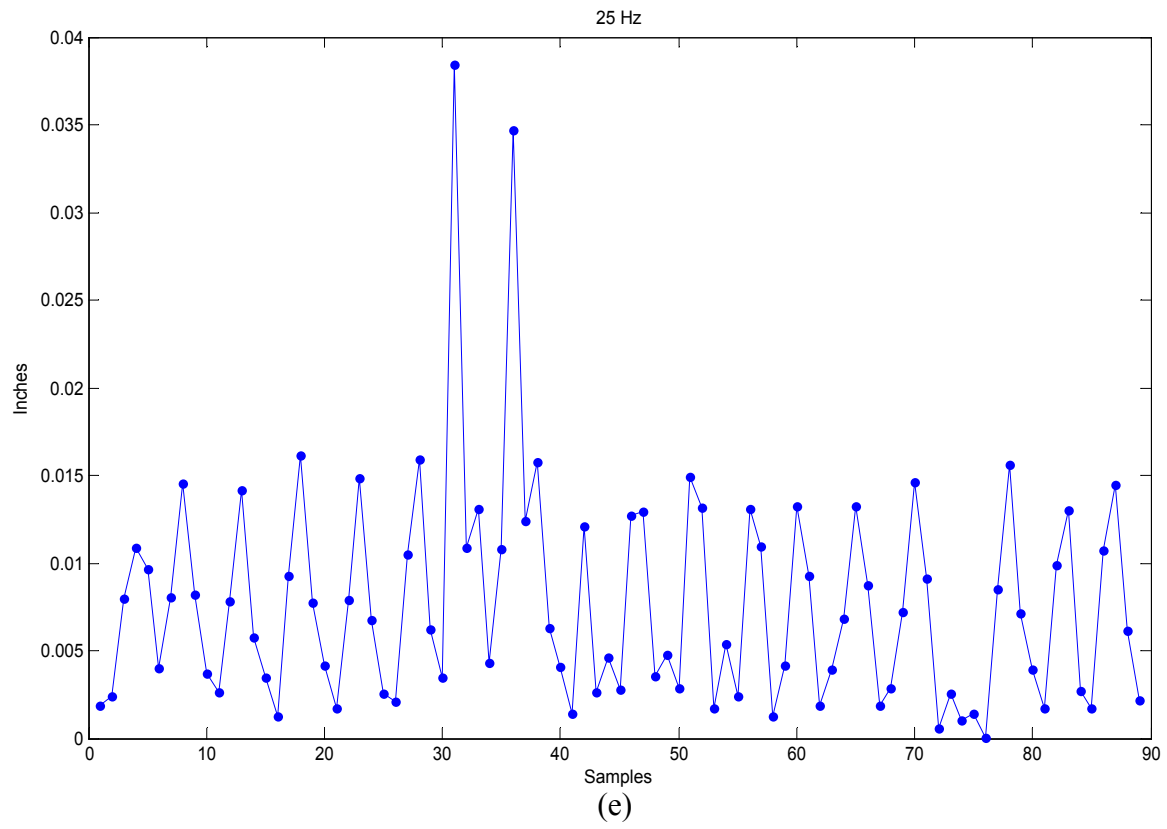


Figure 5.3: Displacement at (a) 5 Hz (b) 10 Hz (c) 15 Hz (d) 20 Hz (e) 25 Hz and (f) 30 Hz.

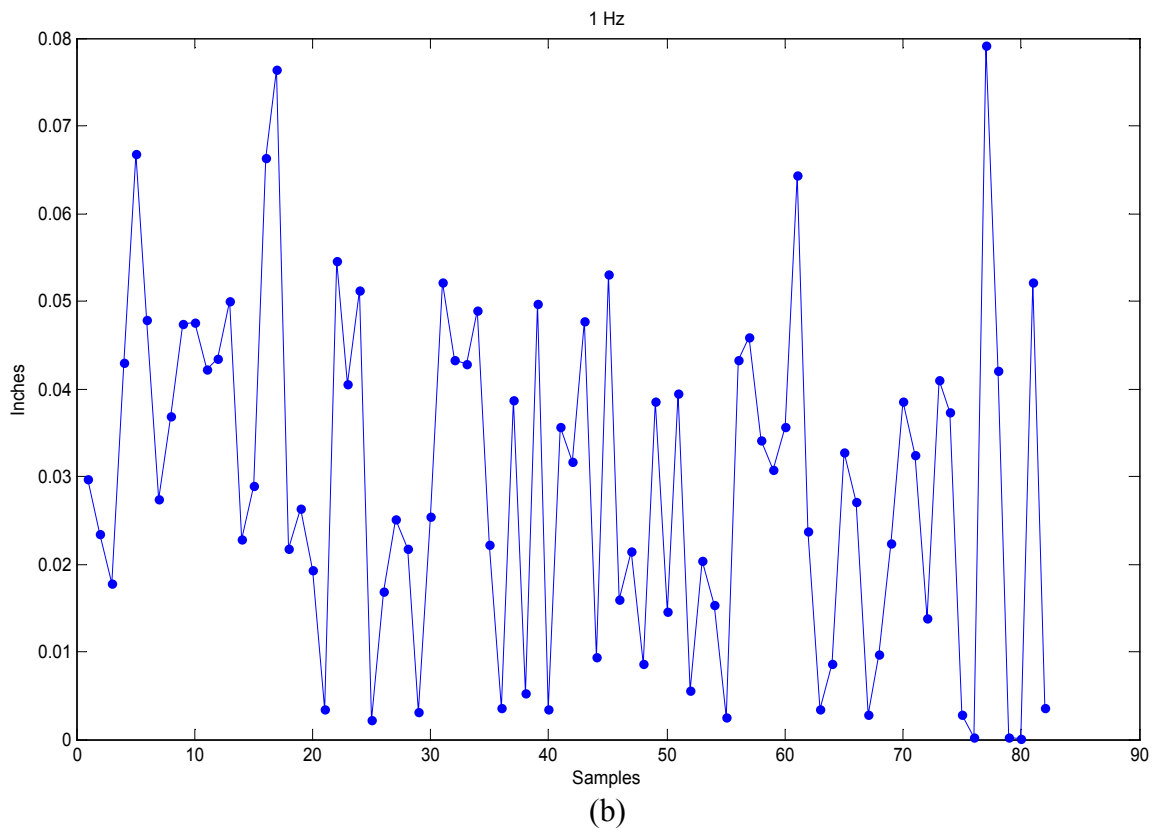
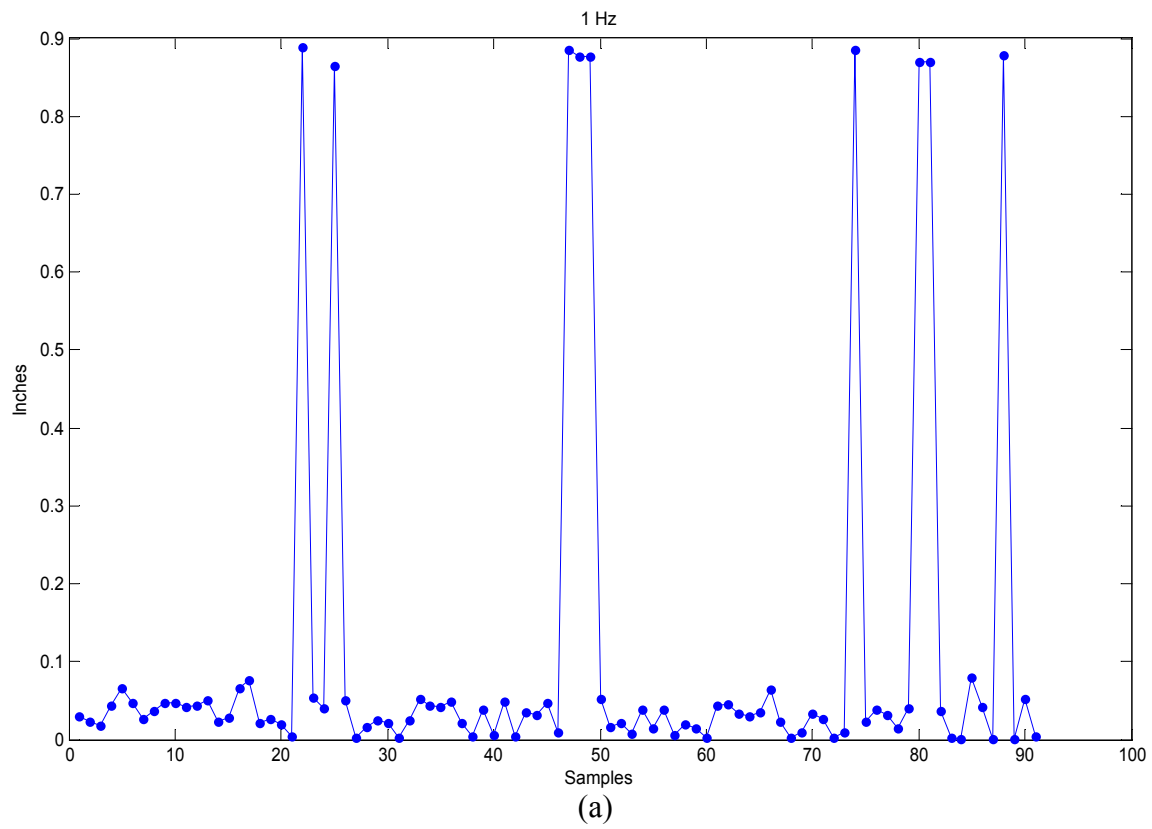


Figure 5.4: Displacement at (a) 1 Hz and (b) Effects of the ADXL202 Noise Floor.

5.2 ASIC Layout

Having verified the functionality of the double integration algorithm, the layout of an ASIC is created using Cadence Encounter (Fig. 5.5). The result is a device with an area of 0.04 mm². Using equation 25 to estimate the number of die per wafer, where S is the area of the die and d is the diameter of the wafer in millimeters, over 783,100 devices can be produced on an 8-inch wafer. Moreover, the device can be available for fewer than 50 cents compared to the average \$2.25 for an 8-bit microcontroller, allowing for higher placement densities at a lower cost. A summary of the design details reported by the Encounter RTL compiler is given in Table 5.1.

$$DPW = d\pi(\frac{d}{4S} - \frac{1}{\sqrt{2S}}) \quad (25)$$

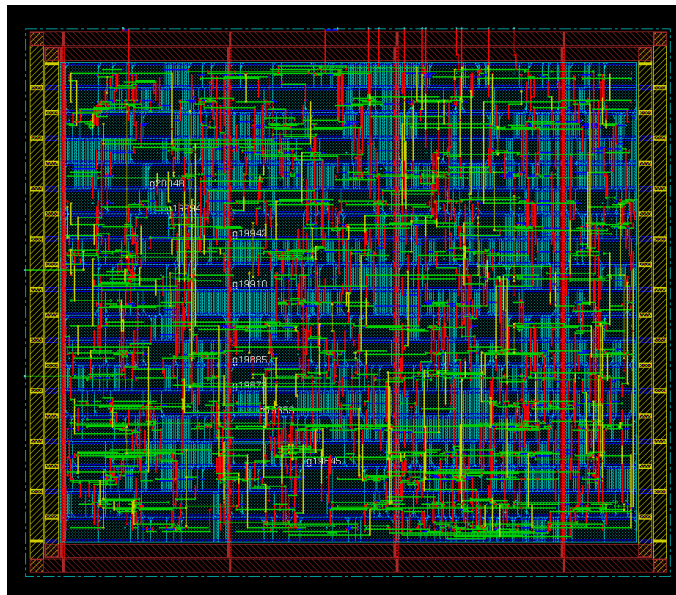


Figure 5.5: AISC Layout.

Table 5.1: ASIC Detail Summary.

Detail	Value
Leakage Power (nW)	316.291
Dynamic Power (nW)	346325.423
Timing Slack (ps)	397263
Total Number of Gates	614

According to the RTL compiler power report, the total power consumption of the ASIC is well below 1mW. Using the ASIC as a computational core and a UHF transmitter like the one ATA8401 from Atmel, the total power of the sensor circuit is just under 30 mW (table 5.2). This represents an 80% reduction in power with respect to the sensor prototype used for validation and a 60% reduction in comparison to 75 mW consumed by a fully active WISAN node. Considering the sensor acquires and transmits data within one second, the device requires approximately 30 mJ to operate. Assuming no energy losses, current RF energy harvesting technology could be used to provide this amount of energy to power the device. Nevertheless, further research is necessary to determine the amount of energy required to power a device embedded under the surface of concrete.

Table 5.2: Power Characteristics of the Ultra-Low Power Sensor.

Component	Operating Power (mW)
ADXL202	1.98
ASIC	0.3466
ATA8401	27
Total	29.33

Chapter 6: Conclusion and Future Work

6.1 Conclusion

The implementation of novel and inexpensive methods to automatically monitor the structural health of bridges and highways is critical to the efficient allocation of funds towards infrastructure maintenance and development projects. This thesis has proposed the design of an ultra-low power sensor intended to be the basis of a long-term monitoring system to remotely assess the condition of roads. The research explored the implementation of a simple algorithm to obtain maximum displacement figures from acceleration data collected with the ADXL202 MEMS accelerometer. In order to limit the power consumption of the computational core of the sensor, the algorithm was designed to carry out the accumulation component of a double numerical integration method. All multiplication operations necessary to convert the output of the algorithm to displacement values expressed in inches were relegated to a host computer. A reconfigurable sensor prototype based on the Xilinx XC3S250E Spartan 3E FPGA was built and exposed to sinusoidal vibration to validate the functionality of the algorithm. Although the characteristics of sinusoidal vibration presented some challenges for the identification of peak-to-peak displacement, results showed that the sensor prototype successfully produced figures proportional to displacement at frequencies between 5 and 30 Hz.

This research work also presented the layout and characteristics of an ASIC based on the double integration algorithm. The ASIC was proposed as a low-power alternative to commercially available microcontrollers and FPGAs currently used in the design of wireless sensors. The reported total power consumption of the device was well under 1mW. Moreover, an estimated 40% decrease in power consumption was achieved by replacing the computational core of the sensor prototype with the proposed ASIC. This reduction in power consumption is a

key milestone in the development of a long-term monitoring system powered with RFID energy harvesting technology.

6.2 Future Work

Given that the vibration produced by the impact of tires against a road is classified as random, additional testing is required to validate the performance of the double integration algorithm for random acceleration excitation. An analysis can be performed to gauge the impact of initial conditions of random vibration components on the accuracy of the sensor and the ability to identify peak-to-peak displacement from one second of acceleration data. In addition, work should be done to include temperature information in the design of the sensor as the DCM output of the ADXL202 is temperature dependent. Changes in the design to account for temperature fluctuations are crucial to the computation of accurate displacement values. Finally, work should be initiated to explore the use of available RFID energy harvesting technology to power the proposed sensor.

Works Cited

- Analog Devices. 1999. ADXL202/ADXL210 data sheet. http://www.analog.com/static/imported-files/data_sheets/ADXL202_210.pdf
- Andringa, M. M., Neikirk, D. P., and Wood, S. L. 2004. Unpowered wireless analog resistance sensor. Smart Structures and Materials: Sensors and Smart Structures Technologies for Civil, Mechanical, and Aerospace Systems, San Diego, CA, March 15–18. Proceedings of the SPIE. 5391:356–367.
- Bâzu, M., Gălăţeanu, L., Ilian, V. E., Loicq, J., Habraken, S., and Collete J. 2007. Quantitative accelerated life testing of MEMS accelerometers. Sensors. 7(11):2846-2859.
- Bennett R., Hayes-Gill B., Crowe J., Armitage R., Rodgers D., and Hendroff A. 1999. Wireless monitoring of highways. Smart Systems for Bridges, Structures, and Highways Conference, Newport Beach CA, March 1-2. *Proceedings of the SPIE*. 3671:173–182.
- Chen, W., Wen, Z., and Wang, J. 2007. Implementation of 2-axis circular interpolation for a FPGA-based 4-axis motion controller. IEEE International Conference on Control and Automation (ICCA), May 30-June 1. 600-605.
- Chintalapudi, K., Fu, T., Paek, J., Kothari, N., Rangwala, S., Caffrey, J., Govindan, R., Johnson, E., and Masri, S. 2006. Monitoring civil structures with a wireless sensor network. IEEE Internet Computing. 10(2):26-34.
- Chung, H-C., Enotomo, T., Loh, K., and Shinozuka, M. 2004. Real-time visualization of bridge structural response through wireless MEMS sensors. Testing, Reliability, and Application of Microand Nano-Material Systems II, San Diego, CA, March 15–17. Proceedings of SPIE. 5392:239–246.
- Das, N. K., Khorrami, F., and Nourbakhsh, S. 1998. A new integrated piezoelectric–dielectric microstrip antenna for dual wireless actuation and sensing functions. Smart Electronics and MEMS, San Diego, CA, March 2–4. Proceedings of the SPIE. 3328:133–146.
- Digilent. 2007. Digilent Basys Board reference manual. http://www.digilentinc.com/Data/Products/BASYS/BASYS_E_RM.pdf
- Elexol. 2009. USBMOD4 data sheet. <http://www.elexol.com/Download/documents/USBMOD4DS2.PDF>
- Federal Highway Administration. 2006. Status of the nation's highways, bridges and transit: conditions and performance - Report to congress. <http://www.fhwa.dot.gov/policy/2006cpr/index.htm>.
- Goldman, S. 1999. Vibration spectrum analysis. P. 11.

- Hajek, J., Blaney, C., and Hein, D. K. 2006. Mitigation of highway traffic-induced vibration. Annual Conference and Exhibition of the Transportation Association of Canada, Charlottetown, Prince Edward Island.
- Hsieh, K. H., Halling, M. W., Barr, P. J. 2006. Overview of vibrational structural health monitoring with representative case studies. Journal of Bridge Engineering. 11(6):707-715.
- Hunaidi, O. 2000. Traffic vibrations in buildings. Construction Technology Update N0.39.
- Jung, K., Bredow, J. W., and Joshi, S. P. 1999. Electromagnetically coupled embedded sensors. Industrial and Commercial Applications of Smart Structures Technologies, Newport Beach, CA, March 2–4. *Proceedings of the SPIE*. 3674:148–156.
- Kottapalli, V. A., Kiremidjian, A. S., Lynch, J. P., Carryer, E., Kenny, T. W., Law, K. H., and Lei, Y. 2003. Two-tiered wireless sensor network architecture for structural health monitoring. Smart Structures and Materials, San Diego, CA, March 3–6. *Proceedings of the SPIE*. 5057:8–19.
- Labworks Inc. 2009. Sine vibration testing. http://www.labworks-inc.com/enginfo/sine_vib_test.htm.
- Lynch, J. P., Law, K. H., Kiremidjian, A. S., Kenny, T. W., Carryer, E., and Partridge, A. 2001. The design of a wireless sensing unit for structural health monitoring. Proceedings of the 3rd International Workshop on Structural Health Monitoring, Stanford, CA, September 12–14.
- Lynch, J. P., Law, K. H., Kiremidjian, A. S., Kenny, T. W., and Carryer, E. 2002a. A wireless modular monitoring system for civil structures. Proceedings of the 20th International Modal Analysis Conference (IMAC XX), Los Angeles, CA, February 4–7, 1–6.
- Lynch, J. P., Law, K. H., Kiremidjian, A. S., Carryer, E., Kenny, T. W., Partridge, A., and Sundararajan, A. 2002b. Validation of a wireless modular monitoring system for structures. Smart Structures and Materials: Smart Systems for Bridges, Structures, and Highways, San Diego, CA, March 17–21. *Proceedings of the SPIE*. 4696(2): 17–21.
- Lynch, J. P., Sundararajan, A., Law, K. H., Kiremidjian, A. S., Carryer, E., Sohn, H., and Farrar, C. R. 2003. Field validation of a wireless structural health monitoring system on the Alamosa Canyon Bridge. Smart Structures and Materials: Smart Systems and Nondestructive Evaluation for Civil Infrastructures, San Diego, CA, March 3–6. *Proceedings of the SPIE*. 5057:267–278.
- Lynch, J. P., and Loh, K. J., 2006. A summary review of wireless sensors and sensor networks for structural health monitoring. The Shock and Vibration Digest. 38(2):91-128.
- Mascareñas, D., Flynn, E., Todd, M. 2008. Wireless Sensor Technologies for monitoring civil structures. Sound and Vibration. April.

- Mastroleon, L., Kiremidjian, A. S., Carryer, E., and Law, K. H. 2004. Design of a new power-efficient wireless sensor system for structural health monitoring. Non-destructive Detection and Measurement for Homeland Security II, San Diego, CA, March 16–17. *Proceedings of the SPIE*. 5395:51–60.
- Mita, A., and Takhira, S. 2003. A smart sensor using a mechanical memory for structural health monitoring of a damage-controlled building. Smart Materials and Structures. 12(2):204–209.
- Novak, L. J., Grizzle, K. M., Wood, S. L., and Neikirk, D. P. 2003. Development of state sensors for civil engineering structures. Smart Structures and Materials: Smart Systems and Non-destructive Evaluation for Civil Infrastructures, San Diego, CA, March 3–6. *Proceedings of the SPIE*. 5057:358–363.
- Powercast. 2009. Wireless sensor networks. <http://www.powercastco.com/applications/wireless-sensor-networks/>.
- Powercast. 2009. Wireless power for battery-free wireless sensors. Sensor Expo and Conference. <http://powercastco.com/PDF/2009SensorsExpo2.pdf>.
- Saafi, M. and Romine, P. 2004. Embedded MEMS for health monitoring and management of civil infrastructure. Smart Structures and Materials: Sensors and Smart Structures Technologies for Civil, Mechanical, and Aerospace Systems, San Diego, CA, March 15–18. *Proceedings of the SPIE*. 5391:331–343.
- Sazonov, E., Janoyan, K., and Jha, R. 2004. Wireless intelligent sensor network for autonomous structural health monitoring. Smart Structures and Materials: Smart Sensor Technology and Measurement Systems, San Diego, CA, March 15–17. *Proceedings of the SPIE*. 5384:305–314.
- Simonen, J. T., Andringa, M. M., Grizzle, K. M., Wood, S. L., and Neikirk, D. P. 2004. Wireless sensors for monitoring corrosion in reinforced concrete members. Smart Structures and Materials: Sensors and Smart Structures Technologies for Civil, Mechanical, and Aerospace Systems, San Diego, CA, March 15–18. *Proceedings of SPIE*. 5391:587–596.
- Sukun K., Pakzad, S., Culler, D., Demmel, J., Fenves, G., Glaser, S., and Turon, M. 2007. Health monitoring of civil infrastructures using wireless sensor networks. 6th International Symposium on Information Processing in Sensor Networks (IPSN), April 25 - 27. 254 - 263.
- Watters, D. G., Jayaweera, P., Bahr, A. J., Huestis, D. L., Priyantha, N., Meline, R., Reis, R., and Parks, D. 2003. Smart Pebble: wireless sensors for structural health monitoring of bridge decks. Smart Structures and Materials, San Diego, CA, March 3–6. *Proceedings of the SPIE*. 5057:20–28.

- Yang, W., Lynch, J. P., and Law, K. H. 2005. Design of a low-power wireless structural monitoring system for collaborative computational algorithms. 12th Annual International Symposium on Nondestructive Evaluation for Health Monitoring and Diagnostics, San Diego, CA, March 6-10. *Proceedings of the SPIE*. 5768:106.
- Yu, B. X., and Yu, X. 2006. Vibration-based system for pavement condition evaluation. ASCE Conference Proceedings. 183-189.

Appendix A: Verilog Code

```
/////////////////////////////////////////////////////////////////
//
// Create Date: 19:17:34 08/08/2009
// Design Name: dsplcmnt
// Module Name: dsplcmnt
// Project Name: Double Integration Algorithm
// Target Devices: XC3S250E - TQ144
// Tool versions:
// Description:
//
//
// Revision:
// Revision 0.01 - File Created
// Additional Comments:
//
/////////////////////////////////////////////////////////////////
module dsplcmnt(
    clk,
    rst,
    xout,
    tx,
    wr,
    data_out
);

    /*******Inputs/Outputs*****/
    input clk;
    input rst;
    input xout;
    input tx;
    output wr;
    output [7:0] data_out;

    /*******Internal Registers*****/
    reg IN_x1;
    reg IN_x2;
    reg [9:0] one_sec;
    reg [23:0] temp_cnt;
    reg [23:0] T1_rest;
    reg [23:0] T1;
    reg [23:0] accel;
    reg [23:0] vel_tmp;
    reg [23:0] disp_tmp;
    reg [23:0] min_disp;
```

```

reg [23:0] max_disp;
reg [23:0] dsplcmnt;
reg [1:0] sel;
reg [1:0] next;
reg [3:0] wr_en;
reg [7:0] data_out_tmp;
wire wr_reset;
wire pos_edge;
wire neg_edge;
wire negative;

reg [3:0] clk_counter;
/*****Clock Divider – 25MHz to 2.5MHz*****/

wire   clk_reset = (clk_counter == 9);
wire   slow_clk  = (clk_counter < 5);

always @(posedge clk)
begin
    if(clk_reset) clk_counter <= 0;
    else          clk_counter <= clk_counter + 1;
end

/*****Capture input signal from accelerometer*****/

always @(posedge slow_clk)
begin
    if(!rst) begin
        IN_x1 <= 1'b0;
        IN_x2 <= 1'b0;
    end
    else begin
        IN_x1 <= xout;
        IN_x2 <= IN_x1;
    end
end

/*****Set T2 register*****/

always @(posedge slow_clk)
begin
    T1_rest <= 24'h03DE;
end

```

```
/******One-second timer******/
```

```
always @(posedge slow_clk)
begin
    if(!rst) begin
        one_sec <= 10'b0000000000;
    end
    else begin
        if((pos_edge) && (one_sec < 10'h3E8))
            one_sec <= one_sec + 1'b1;
        else if(!pos_edge ) && (one_sec < 10'h3E8))
            one_sec <= one_sec;
        else
            one_sec <= 10'b0000000000;
    end
end
```

```
/******Counter to measure T1 pulse******/
```

```
always @(posedge slow_clk)
begin
    if(!rst) begin
        T1 = 24'h000000;
        temp_cnt = 24'h000000;
    end
    else begin
        if(IN_x1) begin
            T1 = T1;
            temp_cnt = temp_cnt + 1'b1;
        end
        else begin
            if(temp_cnt != 24'h000000)
                T1 = temp_cnt;
            else
                T1 = T1;
                temp_cnt = 24'h000000;
            end
        end
    end
end
```

```
/******Compute acceleration at the end of pulse T1******/
```

```
always @(posedge slow_clk)
begin
```

```

    if(!rst)
        accel <= 24'h0000000;
    else begin
        if(neg_edge)
            accel <= T1 - T1_rest;
        else
            accel <= accel;
    end
end

```

/******Compute velocity at the end of pulse T1 – First accumulator*****/

```

always @(posedge slow_clk)
begin
    if(!rst)
        vel_tmp <= 24'b0000000;
    else begin
        if((neg_edge) && (one_sec < 10'h3E8))
            vel_tmp <= vel_tmp + accel;
        else if(!neg_edge) && (one_sec < 10'h3E8))
            vel_tmp <= vel_tmp;
        else
            vel_tmp <= 24'h0000000;
    end
end

```

/******Compute displacement at the end of pulse T1 – Second accumulator*****/

```

always @(posedge slow_clk)
begin
    if(!rst)
        disp_tmp <= 24'h0000000;
    else begin
        if((neg_edge) && (one_sec < 10'h3E8))
            disp_tmp <= disp_tmp + vel_tmp;
        else if(!neg_edge) && (one_sec < 10'h3E8))
            disp_tmp <= disp_tmp;
        else
            disp_tmp <= 24'h0000000;
    end
end

```

/******Compare and update the maximum and minimum displacement values*****/

```

always @(posedge slow_clk)
begin
    if(!rst) begin
        max_disp <= 24'h000000;
        min_disp <= 24'h000000;
    end
    else begin
        if((neg_edge) && (one_sec < 10'h3E8)) begin
            if(!negative) && (disp_tmp > max_disp)) begin
                max_disp <= disp_tmp;
                min_disp <= min_disp;
            end
            else if(negative) && ((~disp_tmp+ 1'b1) > max_disp)) begin
                max_disp <= max_disp;
                min_disp <= (~disp_tmp) +1'b1;
            end
            else begin
                max_disp <= max_disp;
                min_disp <= min_disp;
            end
        end
        else if(!neg_edge) && (one_sec < 10'h3E8)) begin
            max_disp <= max_disp;
            min_disp <= min_disp;
        end
        else begin
            max_disp <= 24'h000000;
            min_disp <= 24'h000000;
        end
    end
end

/*****Compute pk-pk displacement from maximum and minimum values after one
second*****/
always @(posedge slow_clk)
begin
    if(!rst)
        dspcmnt <= 24'h000000;
    else begin
        if(one_sec == 10'h3E8)
            dspcmnt <= max_disp + min_disp;
        else
            dspcmnt <= dspcmnt;
        end
    end
end

```

```

/*****State machine to output a 24-bit displacement value into three 8-bit sections*****/

```

```

always @(posedge slow_clk)
begin
    if(!rst)
        wr_en <= 0;
    else begin
        if(((one_sec == 10'h3E8)|| (wr_en > 4'h0))&&(tx == 1'b0)) begin
            if(wr_reset)
                wr_en <= 0;
            else
                wr_en <= wr_en + 1;
        end
    end
    wr_en <= 0;
end
end

```

```

always @(posedge slow_clk)
begin
    if(!rst)
        sel <= 2'b00;
    else
        sel <= next;
end

```

```

always @(posedge slow_clk)
begin
    if(!rst) begin
        data_out_tmp <= 8'b00000000;
        next <= 2'b00;
    end
    else begin
        if(wr) begin
            case(sel)
                2'b00:begin
                    data_out_tmp <= 8'h23;
                    next <= 2'b01;
                end
                2'b01:begin
                    data_out_tmp <= dsplcmnt[7:0];
                    next <= 2'b10;
                end
                2'b10:begin
                    data_out_tmp <= dsplcmnt[15:8];

```

```

        next <= 2'b11;
    end
    2'b11:begin
        data_out_tmp <= dsplcmnt[23:16];
        next <= 2'b00;
    end
    default:    begin
        data_out_tmp <= 8'h00;
        next <= 2'b00;
    end
endcase
end
else begin
    data_out_tmp <= data_out_tmp;
    next <= next;
end
end
end
end

/**********Find rising and falling edges of T1 pulse*****/
assign pos_edge = IN_x1 & ~IN_x2;
assign neg_edge = ~IN_x1 & IN_x2;

/**********Indicate when displacement value is negative*****/
assign negative = disp_tmp[23];

/**********Control write enable pulses to send each 8-bit output to USBMOD4*****/
assign wr_reset = (wr_en == 4'hE);
assign wr = ((wr_en == 4'h1)||(wr_en == 4'h2)||(wr_en == 4'h5)||(wr_en == 4'h6)||(wr_en ==
4'h9)||(wr_en == 4'hA)||(wr_en == 4'hD)||(wr_en == 4'hE));
//assign wr = ((wr_en == 4'h1)||(wr_en == 4'h2)||(wr_en == 4'h5)||(wr_en == 4'h6)||(wr_en ==
4'h9)||(wr_en == 4'hA)||(wr_en == 4'hD)||(wr_en == 4'hE));
assign data_out = data_out_tmp;

endmodule

```

Appendix B: ASIC Reports

Power Report

```

=====
Generated by:          Encounter(R) RTL Compiler v07.20-
p004_1
Generated on:          Jul 23 2009  01:39:43 PM
Module:                dsp lcmnt
Technology library:    vtv t_tsmc250
Operating conditions:  _nominal_ (balanced_tree)
Wireload mode:         enclosed
Area mode:             timing library
=====

```

		Leakage	Dynamic	Total
Instance	Cells	Power (nW)	Power (nW)	Power (nW)

dsp lcmnt	614	316.291	346325.423	346641.713

Timing Report

```

=====
Generated by:          Encounter(R) RTL Compiler v07.20-
p004_1
Generated on:          Jul 23 2009  01:39:42 PM
Module:                dsp lcmnt
Technology library:    vtv t_tsmc250
Operating conditions:  _nominal_ (balanced_tree)
Wireload mode:         enclosed
Area mode:             timing library
=====

```

Pin	Type	Fanout	Load (fF)	Slew (ps)	Delay (ps)	Arrival (ps)	

(clock vclk)	launch					0	R
temp_cnt_reg[0]/ck				0		0	R
temp_cnt_reg[0]/q	dp_1	4	34.7	133	+268	268	R
g20215/ip2					+0	268	
g20215/op	nand2_2	2	29.9	120	+182	450	F
g20214/ip					+0	450	
g20214/op	inv_2	1	10.0	61	+84	535	R
g20165/ip2					+0	535	
g20165/op	nand2_2	2	26.8	108	+137	672	F
g20164/ip					+0	672	
g20164/op	inv_2	1	10.0	56	+80	751	R

g20150/ip2					+0	751	
g20150/op	nand2_2	2	26.8	111	+134	886	F
g20149/ip					+0	886	
g20149/op	inv_2	1	10.0	57	+81	967	R
g20107/ip2					+0	967	
g20107/op	nand2_2	2	26.8	111	+135	1102	F
g20106/ip					+0	1102	
g20106/op	inv_2	1	10.0	57	+81	1183	R
g20090/ip2					+0	1183	
g20090/op	nand2_2	2	26.8	111	+135	1318	F
g20089/ip					+0	1318	
g20089/op	inv_2	1	10.0	57	+81	1399	R
g20069/ip2					+0	1399	
g20069/op	nand2_2	2	19.0	98	+116	1515	F
g20068/ip					+0	1515	
g20068/op	inv_2	1	10.0	53	+76	1592	R
g20053/ip2					+0	1592	
g20053/op	nand2_2	2	19.0	89	+114	1706	F
g20052/ip					+0	1706	
g20052/op	inv_2	1	10.0	50	+73	1779	R
g20031/ip2					+0	1779	
g20031/op	nand2_2	2	14.2	80	+100	1879	F
g20030/ip					+0	1879	
g20030/op	inv_1	1	5.2	49	+72	1951	R
g20018/ip2					+0	1951	
g20018/op	nand2_1	1	9.3	83	+113	2064	F
g19992/ip2					+0	2064	
g19992/op	xnor2_2	1	10.4	68	+270	2334	F
g19969/ip1					+0	2334	
g19969/op	and3_2	1	4.6	32	+178	2512	F
temp_cnt_reg[10]/ip	dp_1				+0	2512	
temp_cnt_reg[10]/ck	setup			0	+225	2737	R

(clock vclk)	capture					400000	R

Timing slack : 397263ps
 Start-point : temp_cnt_reg[0]/ck
 End-point : temp_cnt_reg[10]/ip

Gates Report

```

=====
Generated by:          Encounter(R) RTL Compiler v07.20-
p004_1
Generated on:          Jul 23 2009 01:39:42 PM
Module:                dsplcmnt
  
```

Technology library: vtv_tsmc250
 Operating conditions: _nominal_ (balanced_tree)
 Wireload mode: enclosed
 Area mode: timing library

=====

Gate	Instances	Area	Library

ABorC	9	1175.731	vtvt_tsmc250
and2_1	94	7674.912	vtvt_tsmc250
and2_2	3	244.944	vtvt_tsmc250
and3_1	7	685.843	vtvt_tsmc250
and3_2	4	391.910	vtvt_tsmc250
and4_1	1	114.307	vtvt_tsmc250
dp_1	93	27335.750	vtvt_tsmc250
fulladder	8	2874.010	vtvt_tsmc250
inv_1	59	2890.339	vtvt_tsmc250
inv_2	8	391.910	vtvt_tsmc250
inv_4	3	146.966	vtvt_tsmc250
mux2_1	36	4115.059	vtvt_tsmc250
nand2_1	41	2678.054	vtvt_tsmc250
nand2_2	9	587.866	vtvt_tsmc250
nand3_1	1	81.648	vtvt_tsmc250
nand4_1	2	163.296	vtvt_tsmc250
nor2_1	115	5633.712	vtvt_tsmc250
nor2_2	3	146.966	vtvt_tsmc250
nor3_1	32	2090.189	vtvt_tsmc250
nor3_2	10	653.184	vtvt_tsmc250
nor4_1	1	81.648	vtvt_tsmc250
nor4_2	1	81.648	vtvt_tsmc250
not_ab_or_c_or_d	9	1028.765	vtvt_tsmc250
or2_1	5	408.240	vtvt_tsmc250
or4_1	3	293.933	vtvt_tsmc250
xnor2_1	4	587.866	vtvt_tsmc250
xnor2_2	5	734.832	vtvt_tsmc250
xor2_1	42	5486.746	vtvt_tsmc250
xor2_2	6	783.821	vtvt_tsmc250

total	614	69564.096	

Type	Instances	Area	Area %

sequential	93	27335.750	39.3
inverter	70	3429.216	4.9
logic	451	38799.130	55.8

total 614 69564.096 100.0

Vita

Karla Enríquez was born in Ciudad Juárez Chihuahua, México. The first daughter of Carla Pacheco, she graduated from Colegio de Bachilleres No. 6 in Ciudad Juarez in the summer of 2002 and entered the University of Texas at El Paso (UTEP) in the fall. While pursuing a bachelor's degree in Electrical and Computer Engineering, she worked as an undergraduate research assistant under the mentorship of Dr. Eric MacDonald. During the NSF/NSB visit to UTEP in February of 2005, she presented a poster on the development of an ultra-low power microcontroller for a micro-gyroscope and presented on this topic again at the first annual SACNAS UTEP Chapter Research Expo in March of 2006. Karla graduated with honors in the summer of 2007 and reentered UTEP as a graduate student to pursue a master's degree in Computer Engineering. She worked as a full time intern for Intel Corporation in Chandler, Arizona between May 2008 and January 2009, and continues to work for the leader in semiconductor chip manufacturing as a part time employee.

Permanent address: 6601 South Karlov
Chicago, IL 60629

This thesis/dissertation was typed by the author.